THE INTERPLAY BETWEEN PROTO–NEUTRON STAR CONVECTION AND NEUTRINO TRANSPORT IN CORE-COLLAPSE SUPERNOVAE

A. MEZZACAPPA,[1,2] A. C. CALDER,[1,3] S. W. BRUENN,[4] J. M. BLONDIN,[5] M. W. GUIDRY,[1,2]
M. R. STRAYER,[1,2] AND A. S. UMAR[3]

ABSTRACT

We couple two-dimensional hydrodynamics to realistic one-dimensional multigroup flux-limited diffusion neutrino transport to investigate proto–neutron star convection in core-collapse supernovae, and more specifically, the interplay between its development and neutrino transport. Our initial conditions, time-dependent boundary conditions, and neutrino distributions for computing neutrino heating, cooling, and deleptonization rates are obtained from one-dimensional simulations that implement multigroup flux-limited diffusion and one-dimensional hydrodynamics.

The development and evolution of proto–neutron star convection are investigated for both 15 and 25 $M_\odot$ models, representative of the two classes of stars with compact and extended iron cores, respectively. For both models, in the absence of neutrino transport, the angle-averaged radial and angular convection velocities in the initial Ledoux unstable region below the shock after bounce achieve their peak values in ~ 20 ms, after which they decrease as the convection in this region dissipates. The dissipation occurs as the gradients are smoothed out by convection. This initial proto–neutron star convection episode seeds additional convectively unstable regions farther out beneath the shock. The additional proto–neutron star convection is driven by successive negative entropy gradients that develop as the shock, in propagating out after core bounce, is successively strengthened and weakened by the oscillating inner core. The convection beneath the shock distorts its sphericity, but on the average the shock radius is not boosted significantly relative to its radius in our corresponding one-dimensional models.

In the presence of neutrino transport, proto–neutron star convection velocities are too small relative to bulk inflow velocities to result in any significant convective transport of entropy and leptons. This is evident in our two-dimensional entropy snapshots, which in this case appear spherically symmetric. The peak angle-averaged radial and angular convection velocities are orders of magnitude smaller than they are in the corresponding "hydrodynamics-only" models.

A simple analytical model supports our numerical results, indicating that the inclusion of neutrino transport reduces the entropy-driven (lepton-driven) convection growth rates and asymptotic velocities by a factor ~ 3 (50) at the neutrinosphere and a factor ~ 250 (1000) at $\rho = 10^{12}$ g cm^{-3}, for both our 15 and 25 $M_\odot$ models. Moreover, when transport is included, the initial postbounce entropy gradient is smoothed out by neutrino diffusion, whereas the initial lepton gradient is maintained by electron capture and neutrino escape near the neutrinosphere. Despite the maintenance of the lepton gradient, proto–neutron star convection does not develop over the 100 ms duration typical of all our simulations, except in the instance where "low-test" intial conditions are used, which are generated by core-collapse and bounce simulations that neglect neutrino–electron scattering and ion–ion screening corrections to neutrino–nucleus elastic scattering.

Models favoring the development of proto–neutron star convection either by starting with more favorable, albeit artificial (low-test), initial conditions or by including transport corrections that were ignored in our "fiducial" models were considered. Our conclusions nonetheless remained the same. Evidence of proto–neutron star convection in our two-dimensional entropy snapshots was minimal, and, as in our fiducial models, the angle-averaged convective velocities when neutrino transport was included remained orders of magnitude smaller than their counterparts in the corresponding hydrodynamics-only models.

Subject headings: convection — stars: interiors — stars: neutron — supernovae: general

1. INTRODUCTION

1.1. *Current Core-Collapse Supernova Paradigm*

The current core-collapse supernova paradigm begins with the collapse of the iron core of an evolved massive star

[1] Theoretical and Computational Physics Group, Oak Ridge National Laboratory, Oak Ridge, TN 37831-6354.

[2] Department of Physics and Astronomy, University of Tennessee, Knoxville, TN 37996-1200.

[3] Department of Physics and Astronomy, Vanderbilt University, Nashville, TN 37235.

[4] Department of Physics, Florida Atlantic University, Boca Raton, FL 33431-0991.

[5] Department of Physics, North Carolina State University, Raleigh, NC 27695-8202.

at the end of its thermonuclear evolution. The rebound of the inner core, brought about by the rapid increase of pressure with density when the density rises above nuclear matter density, generates a shock wave at a radius ~ 20 km, and drives it into the outer core. All groups currently agree that, rather than propagating directly outward through the entire envelope and producing a supernova, the shock stalls and turns into an accretion shock at a radius of 100–200 km. This happens for several reasons: (1) Nuclear dissociation behind the shock lowers the ratio of pressure to energy, thereby lowering the strength of the shock for a given energy delivered to it by the inner core. (2) There is a reduction in both the thermal and lepton number contribu-

tion to the shock pressure as a result of the intense burst of ν_e radiation through the shock that ensues when it passes outwardly through the ν_e sphere, which at this time is located at ~ 60 km.

All groups also currently believe that the supernova is powered by some variant of the "shock-reheating mechanism" of Wilson (1985) and Bethe & Wilson (1985). In this mechanism, the material behind the shock heats on a timescale of hundreds of milliseconds by the transfer and deposition of energy by neutrinos from the hot contracting core. As a result of this energy transfer, the shock is once again driven out. This is in contrast to the original neutrino-driven supernova mechanism of Colgate & White (1966), which operated on the dynamical timescale of milliseconds.

The energy transfer between neutrinos and matter behind the shock is mediated primarily by the charged current reactions $\nu_e + n \rightleftharpoons p + e^-$ and $\bar{\nu} + p \rightleftharpoons n + e^+$. When these reactions proceed to the right, the matter heats; when they proceed to the left, the matter cools. To drive these reactions sufficiently rapidly to the right for a supernova to develop requires a critical combination of ν_e-$\bar{\nu}_e$ luminosity and rms energy (e.g., Burrows & Goshy 1993) that no recent realistic, spherically symmetric, numerical simulation has to date delivered (Bruenn 1993; Cooperstein 1993; Wilson & Mayle 1993).

1.2. *Role of Fluid Instabilities*

A possible way out of this impasse is illuminated by the early recognition that neutrino luminosities and rms energies might be enhanced by fluid instabilities occurring below the neutrinosphere (Epstein 1979; Bruenn, Buchler, & Livio 1979; Colgate & Petschek 1980; Mayle 1985; Wilson et al. 1986; Arnett 1987; Burrows 1987; Burrows & Lattimer 1988), or that the neutrino energy deposition efficiency might be increased by fluid instabilities occurring above the neutrinosphere (Bethe 1990; Herant, Benz, & Colgate 1992; Colgate, Herant, & Benz 1993). Both of these possibilities are being vigorously pursued by a number of groups. Additional motivation for the study of fluid instabilities at this early stage in the development of a supernova is the existence of a large variety of observational hints that large-scale mixing processes occurred in the early phase of the explosion of SN 1987A and played an important role in generating the observables (e.g., see Herant et al. 1992, 1994; Burrows, Hayes, & Fryxell 1995; Janka & Müller 1996).

1.3. *Fluid Instabilities below the Neutrinosphere*

Consider the region in the vicinity of and below the neutrinosphere, which will be the subject of this paper. Material in this region is in nuclear statistical equilibrium, and its thermodynamic state and composition can therefore be specified by just three independent variables. We will choose these to be the dimensionless entropy per baryon, s; the lepton fraction, Y_ℓ; and the pressure, P. Above the neutrinosphere, electrons and neutrinos are no longer strongly interacting and Y_ℓ should be replaced by the electron fraction, Y_e. In the presence of gradients in s and/or Y_ℓ, a strong gravitational field, and the neutrino transport of energy and leptons, the material may be unstable to any one of a number of fluid instabilities (Bruenn & Dineva 1996). If we ignore the effects of neutrino transport for the moment, the situation simplifies and the number of possible fluid insta-

bilities is reduced to one, viz., the Rayleigh-Taylor (convective) instability. Under these conditions, the criterion for convective instability is the Ledoux condition, given by

$$\left(\frac{\partial \rho}{\partial \ln Y_\ell}\right)_{s,P}\left(\frac{\partial \ln Y_\ell}{\partial r}\right) + \left(\frac{\partial \rho}{\partial \ln s}\right)_{Y_\ell,P}\left(\frac{\partial \ln s}{\partial r}\right) > 0 . \quad (1)$$

The derivative $(\partial\rho/\partial \ln s)_{Y_\ell,P}$ is negative for all thermodynamic states; therefore, negative entropy gradients always tend to be destabilizing. On the other hand, the derivative $(\partial\rho/\partial \ln Y_\ell)_{s,P}$ is negative for large Y_ℓ, but becomes positive for small Y_ℓ.[6] The critical value of Y_ℓ at which the derivative changes sign depends on s and P, but is typically in the range 0.1–0.2. Thus, negative gradients in Y_ℓ initially tend to be destabilizing, but become stabilizing when the core deleptonizes sufficiently for values of Y_ℓ to go below the critical value. We will refer to convection driven by negative gradients in s and Y_ℓ near and below the neutrinosphere as "entropy-driven proto–neutron star convection" and "lepton-driven proto–neutron star convection," respectively. These modes of convection are to be distinguished from the entropy-driven convection that occurs above the neutrinosphere after shock stagnation. This convection is sustained by neutrino heating, and will be referred to as "neutrino-driven convection." It will be the subject of another paper (Mezzacappa et al. 1998; see also Herant et al. 1992, 1994; Miller, Wilson, & Mayle 1993; Burrows et al. 1995; Janka & Müller 1996).

If we now bring the neutrino transport of energy and leptons into the picture, entropy- and lepton-driven proto–neutron star convection are still possible (with reduced growth rates), and two additional modes of instability, "neutron fingers" and "semiconvection," become possible. (See Bruenn & Dineva 1996 for a physical description of these instabilities.) These instabilities occur on a diffusion rather than on a dynamical timescale, and usually require that one of the gradients (s or Y_ℓ) be stabilizing while the other is destabilizing, and that energy and lepton equilibration by neutrinos proceed at different rates.

There are several reasons why fluid instabilities in the region below the neutrinosphere may play an important role in the shock-reheating mechanism. All have to do with the fact that instabilities tend to drive fluid motions that tend to circulate the fluid throughout the unstable region. The fluid motions associated with entropy-driven proto–neutron star convection will tend to advect high-entropy material from deeper in the core to the vicinity of the neutrinosphere, increasing the temperature of the neutrinosphere and thereby increasing both the ν_e and the $\bar{\nu}_e$ emission rates. Lepton-driven proto–neutron star convection will tend to advect lepton-rich material from deeper in the core to the vicinity of the neutrinosphere, increasing and decreasing the ν_e and $\bar{\nu}_e$ emission rates, respectively, and hastening the deleptonization of the core.

---

[6] An increase in Y_ℓ implies an increase in the number of particles, and this must be accompanied by a decrease in the temperature T to keep s constant. The increase in particle number tends to increase P, while the decrease in temperature tends to decrease P. At large Y_ℓ, the increase in the number of particles has the more important effect on P, and ρ must decrease to keep P constant. Under these conditions, the derivative $(\partial\rho/\partial \ln Y_\ell)_{s,P}$ is therefore negative. At small Y_ℓ, the decrease in temperature is the more important effect, and ρ must increase to keep P constant, making the derivative positive.

1.4. Lepton-driven Convection

As we will indicate below, if proto–neutron star convection is important for shock reheating, lepton-driven proto–neutron star convection is probably more important than entropy-driven proto–neutron star convection. A negative lepton gradient results from the fact that the region well below the neutrinosphere is lepton rich relative to the material flowing inward through the neutrinosphere at the time of shock stagnation. This is because the latter is completely shock dissociated into free neutrons and protons and is hydrostatically settling onto the core when it passes through the neutrinosphere. Electron capture therefore proceeds rapidly on the plethora of free protons, and plenty of time is available for the v_e's produced by these electron captures to escape. Thus, the material in the vicinity of the neutrinosphere at this time is very lepton poor ($Y_\ell \lesssim 0.1$). On the other hand, material deep within the core passed rapidly through the neutrinosphere during infall, and either never encountered the shock or encountered the shock below the neutrinosphere, as the shock was beginning to form. This material was therefore "cold," and contained only a small mass fraction of free protons when it passed inwardly through the neutrinosphere. As a result, electron capture proceeded more slowly and the v_e's produced by it had less time to escape. Consequently, the material residing deep within the core has a higher lepton fraction ($Y_\ell \sim 0.3$) at the time of shock stagnation, and a negative gradient in Y_ℓ below the neutrinosphere is naturally established. This gradient is maintained by continuing deleptonization near the neutrinosphere.

The negative gradient in Y_ℓ, unless stabilized by a positive gradient in s, will drive a convective flow that may advect leptons from the lepton-rich interior to the vicinity of the neutrinosphere, where they will be radiated away as v_e's. This is the basis of the original suggestion of Epstein (1979), and the early work of Bruenn, Buchler, & Livio (1979), Colgate & Petschek (1980), and Livio, Buchler, & Colgate (1980). Interest in this early work waned when it was pointed out that the positive entropy gradient established by reenergizing the shock would stabilize much of this region (Lattimer & Mazurek 1981; Smarr et al. 1981), and because of the growing interest in the "prompt" supernovae mechanism. However, as the prompt mechanism proved untenable and attention turned to shock reheating, and as SN 1987A appeared with its many hints of fluid instabilities occurring early on, interest in the role of fluid instabilities in the supernova mechanism revived (Arnett 1986, 1987; Bethe 1990, 1993; Bruenn & Mezzacappa 1994; Bruenn, Mezzacappa, & Dineva 1995; Bruenn & Dineva 1996; Burrows 1987; Burows & Lattimer 1988; Burrows & Fryxell 1992, 1993; Burrows et al. 1995; Colgate et al. 1993; Herant et al. 1992; Herant et al. 1994; Janka & Müller 1993a, 1993b, 1995, 1996; Müller 1993; Müller & Janka 1994; Shimizu, Yamada, & Sato 1993, 1994; Wilson & Mayle 1988, 1993).

1.5. Neutron Fingers

The stabilizing effect of the positive entropy gradient established by the shock as it gathers power from the rebounding inner core prompted Mayle and Wilson to invoke neutron fingers as a driver of fluid circulation below the neutrinosphere (Mayle 1985, Wilson et al. 1986, Wilson & Mayle 1988, 1993). Modeling the fluid circulation by a mixing-length algorithm, they found that if the fluid circula-

tion were made sufficiently vigorous, they could generate explosions out of what would otherwise have been duds. Neutron fingers can occur in the presence of a positive entropy gradient and a negative lepton gradient if the energy equilibration rate of a fluid element with the background is faster than the lepton equilibration rate. The opposite was found to be the case, however, in recent investigations by Bruenn et al. (1995), and Bruenn & Dineva (1996). The implication of these investigations is that the material, if unstable at all, will be unstable to semiconvection rather than neutron fingers. Semiconvection tends to drive more localized flows and consequently may not transport leptons efficiently to the neutrinosphere.

1.6. Entropy-driven Convection

While the shock establishes a positive entropy gradient as it gathers strength, Arnett (1986, 1987) pointed out that the dissipation of the shock farther out, owing to nuclear dissociation and v_e radiation, will imprint a negative entropy gradient, and therefore destabilize this region to entropy-driven convection. While Arnett (1986, 1987), Burrows (1987), and Burrows & Lattimer (1988) emphasized the importance of neutrinosphere heating by this convection, the latter two papers pointed out that the transfer of heat to the neutrinosphere from an entropy spike deeper in the core can accelerate mantle collapse and thereby inhibit the outward progress of the shock (see also Bethe, Brown, & Cooperstein 1987).

For entropies exceeding ~ 5, a negative gradient in $\ln s$ is more destabilizing than a negative gradient in $\ln Y_\ell$ of the same magnitude (e.g., Bruenn, Mezzacappa, & Dineva 1995, Fig. 1); therefore, one might expect a vigorous entropy-driven proto–neutron star convection to become established exterior to 0.7–1.0 $M_\odot$ immediately after shock propagation. However, the magnitude and location of the negative entropy gradients established by the dissipating shock depends sensitively on the numerical model used to compute the prior evolution of the core (Bruenn & Mezzacappa 1994, Fig. 1). The more realistic the numerical model, the smaller the magnitude of the negative entropy gradients established by the shock. It is therefore likely that both the magnitude and the extent of the negative entropy gradients established by the shock will be minimal. Once entropy-driven proto–neutron star convection gets established, the convective mixing will tend to flatten the entropy gradient driving it; there is no process maintaining the negative entropy gradient, and the force driving entropy-driven convection will dissipate. Thus, entropy-driven proto–neutron star convection sows the seeds of its own destruction. A final problem with entropy-driven proto–neutron star convection for shock revival is that numerical simulations indicate that conditions favorable for shock revival are not established until ~ 50 ms after bounce (Janka & Müller 1993a; Bruenn & Mezzacappa 1994). On the other hand, multidimensional simulations of entropy-driven proto–neutron star convection show that the convection quickly grows into the nonlinear regime (10–15 ms), and the entropy gradients are flattened in ~ 25–30 ms (Burrows & Fryxell 1992, 1993; Janka & Müller 1993b, 1996; Müller 1993; Müller & Janka 1994). Thus, by the time the region above the neutrinosphere is in a configuration favorable for neutrino-energy deposition, entropy-driven proto–neutron star convection has dissipated. It is therefore unlikely that it will revive the shock. However, it may play a role in seeding

both lepton-driven proto–neutron star convection and neutrino-driven convection. It will also affect the structure of the core and should not be ignored.

1.7. *Current Status of Proto–Neutron Star Convection*

The role played by entropy- and lepton-driven proto–neutron star convection in the supernova mechanism and the evolution of the core is highly unclear and contradictory at the present time. Burrows & Fryxell (1992) found vigorous entropy-driven proto–neutron star convection in two-dimensional hydrodynamics computations that did not include neutrino transport. With the inclusion of gray radial-ray neutrino diffusion they found a "convective trigger," i.e., convectively enhanced neutrino luminosities that triggered an explosion within 20 ms (Burrows & Fryxell 1993). In a later work (Burrows et al. 1995), they report that entropy- and lepton-driven proto–neutron star convection are "weak," and presumably unimportant. Herant et al. (1994) found intermittent and model-dependent lepton-driven convection in a relatively narrow region in the vicinity of the neutrinosphere, and entropy-driven convection farther out—the latter ultimately merging with neutrino-driven convection. Janka & Müller (1993b, 1996), Müller (1993), and Müller & Janka (1994) performed two- and three-dimensional hydrodynamics simulations of proto–neutron star convection with several postcollapse models and found that the convection, while model dependent, is initially vigorous in all cases. In their most recent work they report that convection's purely hydrodynamic effect pushes the shock from its stagnation radius at ∼200 km (one-dimensional initial conditions) out to ∼400 km (two-dimensional case) and to ∼300 km (three-dimensional case). Keil, Janka, & Müller (1996) have recently followed the evolution of a proto–neutron star for more than 1 s with two-dimensional hydrodynamics and radial-ray, gray, equilibrium neutrino diffusion. They found that lepton-driven Ledoux convection continues for a long time and engulfs the entire core after about 1 s. Moreover, they found that the convection increases the neutrino luminosities by up to a factor of 2 and the mean energies of the emitted neutrinos by 10%–20%. Bruenn & Mezzacappa (1994) performed self-consistent one-dimensional simulations of proto–neutron star evolution using multigroup flux-limited diffusion (MGFLD) for neutrino transport and a mixing-length algorithm for convection. In contrast to the results of Keil et al. (1996), they found only mild convective activity inside and around the neutrinosphere for a duration ∼30 ms, although there simulations covered a postbounce period of 0.5 s. While one may argue that the mixing-length approximation fails to reproduce all of the properties of the convective flow, it is nevertheless sensitive to any Ledoux instabilities, and would trace out these instabilities as they develop.

1.8. *This Work*

Part of the reason for the present confusion concerning the vigor and extent of proto–neutron star convection and its role in the supernova mechanism is that numerically simulating this convection is a very difficult problem in radiation hydrodynamics. Neutrinos and matter are strongly coupled in this regime, and it can be expected that neutrino transport will have a profound influence on both the character and the growth rate of any fluid instability. Different initial postcollapse models and alternative approximations to the neutrino transport can produce widely varying results. A self-consistent calculation of proto–neutron star convection requires that both the hydrodynamics and the neutrino transport be multidimensional. Only Herant et al. (1994) have performed such calculations, although their neutrino transport was much simpler than the transport used in sophisticated one-dimensional codes. Helpful insights into the nature and growth rates of fluid instabilities in this regime can be obtaind by semianalytical investigations that are now in progress (Bruenn & Dineva 1997).

In this paper we investigate proto–neutron star convection with a numerical scheme that is a vast improvement over the one-dimensional scheme used by Bruenn & Mezzacappa (1994). Here we couple two-dimensional piecewise parabolic method (PPM) hydrodynamics with realistic one-dimensional MGFLD. Computations of proto–neutron star convection that ignore neutrino transport or that implement radial-ray neutrino transport ignore the tendency of transport to equilibrate upflows and downflows with each other in energy and leptons, thus reducing the very buoyancy contrast driving these flows. We show by a simple analytical example that these computations therefore overestimate the growth rates and final amplitude of proto–neutron star convection. Our one-dimensional neutrino transport represents an alternative intermediate step (compared with radial-ray neutrino transport) along the way to full multidimensional transport. One-dimensional transport obtains in the limit in which the neutrino transport in the tangential direction is rapid enough to render the neutrino fields spherically symmetric, and therefore, in this regard, is complementary to radial-ray transport. It is also important to note that our neutrino transport is multigroup, rather than gray, which becomes particularly important near the neutrinospheres, where the matter becomes semitransparent to neutrinos and where gray transport would not be adequate.

In § 2, we describe our hydrodynamics code, Extended Virginia Hydrodynamics-1 (EVH-1); our procedure coupling neutrino transport to EVH-1; and the models used to initiate the simulations. In § 3, we present the results of our simulations. The tendency of energy and lepton transport by neutrinos to suppress proto–neutron star convection, which is the central feature in all of our numerical results, is discussed with the aid of a simple analytical model in § 4. A summary of our work and of its implications is given in § 5.

2. INITIAL MODELS AND METHODOLOGY

2.1. *Overview*

In this work, all simulations begin with either the 15 $M_\odot$ or the 25 $M_\odot$ precollapse models, S25s7b or S15s7b, provided by Woosley (Woosley & Weaver 1995; Weaver & Woosley 1998). These initial models were evolved through core collapse and bounce using MGFLD neutrino transport and one-dimensional Lagrangian hydrodynamics (Bruenn 1985). These one-dimensional simulations were continued approximately 700 ms after bounce for the purpose of generating boundary and neutrino distribution data to be used in our two-dimensional simulations, as described below. At a simulation time of typically tens of milliseconds after bounce, the one-dimensional configurations were mapped onto a two-dimensional Eulerian grid. The inner and outer boundaries of the two-dimensional grid

were chosen to be at radii of 20 and 1000 km, respectively, for all runs. These choices set the inner and outer boundaries well below and above the unstable regions at the onset of the simulations. The grids used 128 nonuniform radial spatial zones. This gave sufficient resolution at the inner boundary and at the shock. The nonuniform zoning was varied until, for a test simulation, excellent agreement was seen between one-dimensional runs using 128 nonuniform and 512 uniform zones (see Figs. 2c and 2d). One hundred and twenty-eight uniform angular zones spanning a range of 180° were used for θ. With the assumption of axisymmetry, the range of 180° spans the entire physical space, and, accordingly, reflecting boundary conditions are used on the polar axis.

Because the finite differencing in our PPM scheme is nearly noise free, and because we cannot rely on machine roundoff to seed convection in a time that is short compared with the hydrodynamics timescales in our runs, we seeded convection in the Ledoux-unstable regions below and around the neutrinospheres by applying random velocity perturbations to the radial and angular velocities between ±5% of the local sound speed. This is consistent with seeding used by other groups. Moreover, in a two-dimensional simulation of convection during the shell burning of oxygen prior to core collapse, Bazan & Arnett (1994) found inhomogeneities of density, temperature, pressure, and electron fraction ~5%, 1%, 3%, and 0.08%, respectively, and convection velocities ~15% of the local sound speed. Therefore, our seeding choice seems reasonable, although a more systematic study should be carried out.

The two-dimensional hydrodynamics was evolved using EVH-1, an extended version of the PPM hydrodynamics code VH-1. One of the extensions allows for coupling to general equations of state. For the most part, matter in our simulations is in nuclear statistical equilibrium (NSE), and to describe its thermodynamic state we use the equation of state provided by Lattimer & Swesty (1991). However, below a density and temperature threshold, the code switches to a non-NSE equation of state. If a zone falls below the density or temperature threshold of 1.674×10^7 g cm^{-3} or 0.3447 MeV, respectively, it is "deflashed" to silicon while conserving energy within the zone. This is well outside the convectively unstable region, and deflashing was therefore performed in a spherically symmetric manner. An ideal gas equation of state, plus internal degrees of freedom to mimic the NSE equation of state and to provide a more seamless transition to non-NSE, is then used to describe the silicon in its subsequent evolution. As will be described in detail later, with both equations of state, tables of thermodynamic quantities are constructed at the beginning of a simulation, and as the calculation proceeds, the code interpolates within these tables.

At each time step in the two-dimensional evolution, the results of the corresponding one-dimensional MGFLD run, completed at a prior time, provide spherically symmetric time-dependent boundary data for our inner and outer two-dimensional boundaries, and neutrino distributions for the local neutrino heating, cooling, and matter deleptonization everywhere on our two-dimensional grid. The boundary data consist of enclosed mass, radial velocity, density, temperature, electron fraction, pressure, and specific internal energy, and values at our fixed inner Eulerian radius were extracted from the one-dimensional Lagrangian data by

interpolation in r and t. A call to the equation of state provides the boundary value of the first adiabatic index, which is required by our PPM scheme. The outer boundary data were specified in the same way. The neutrino heating and cooling and the matter deleptonization were computed at each time step using tables of ψ_i^0's in r, t, and E_v, constructed from our one-dimensional simulations. [$\psi_i^0(r, t, E_v)$ are the zeroth moments of the neutrino distribution functions; i is a neutrino flavor index.] Ideally, the neutrino–matter momentum transfer should also be included. However, this is a small correction to the matter pressure.

Gravity was assumed to be Newtonian and spherically symmetric in our two-dimensional simulations. The justification for the latter is the fact that the gravitational field in the convectively unstable region was dominated by the spherically symmetric enclosed mass at the region's base. The time dependence of the mass enclosed by our inner boundary, given by our one-dimensional MGFLD runs, was taken into account. The contribution to the gravitational field of the mass on the grid was calculated at each time step by finding the angle-averaged density in a shell between radial grid points, and summing the masses of the shells up to a particular radial grid point. (The solution of the Poisson equation for the gravitational potential will be incorporated in future investigations.)

Comparisons were made (see below) to ensure that in one dimension the results from our code matched the results obtained with the MGFLD code, modulo EVH-1's better resolution of the shock.

2.2. Details of the Simulations

Table 1 contains the initial times for, and a brief description of, each simulation. All of the simulations listed below were performed with the PPM code, and began a few milliseconds after bounce. The one-dimensional PPM simulations were performed for the purpose of comparison with our one-dimensional MGFLD simulations.

In simulations B, D, J, and L, the electron neutrino and electron antineutrino distributions ($\psi_{v_e, \bar{v}_e}^0$) used to compute the local neutrino heating, cooling, and matter deleptonization are generated by our accompanying one-dimensional simulations that include all neutrino flavors and interactions. Neutrino–electron scattering (NES) and ion–ion screening corrections are included.

Simulations F, G, and H were initiated from a model whose prior evolution involved a less rigorous treatment of neutrino transport, and were dubbed our "low-test" runs. In particular, the initial model for these runs was evolved through bounce by the MGFLD code, neglecting NES and ion–ion screening corrections. This less rigorous treatment of neutrino transport provides initial conditions for the two-dimensional simulations that are more conducive to the development of proto–neutron star convection because a larger entropy gradient is established by the weakening of an originally stronger shock.

To explain the way the neutrino distributions are used to calculate the local neutrino heating, cooling, and deleptonization, we must describe how EVH-1 carries out the simulations.

EVH-1 performs the hydrodynamics evolution in sweeps over the grids. In the one-dimensional case, there is a sweep in the radial direction. In the two-dimensional case, there is a sweep first in the radial direction for each angle and then in the angular direction for each radius. In a particular

TABLE 1
SIMULATION START TIMES AND DESCRIPTIONS

Simulation	Initial Time (ms)	Postbounce Time (ms)	Dimensions	Description
25 $M_\odot$ Models				
A	297.9	8.3	1	Hydro only
B	297.9	8.3	1	Hydro + v transport
C	297.9	8.3	2	Hydro only
D	297.9	8.3	2	Hydro + v transport
E	297.9	8.3	2	Finite-time hydro + v
F	299.4	7.23	2	Low-test hydro only
G	299.4	7.23	2	Low-test hydro + v
H	299.4	7.23	2	Finite-time low-test hydro + v
15 $M_\odot$ Models				
I	211.1	11.9	1	Hydro only
J	211.1	11.9	1	Hydro + v transport
K	211.1	11.9	2	Hydro only
L	211.1	11.9	2	Hydro + v transport

sweep, there are four principal variables that evolve. These are density (ρ), temperature (T), electron fraction (Y_e), and specific internal energy (ϵ). (Y_e in a zone changes as a result of hydrodynamic advection, in addition to transformations between e^-'s, e^+'s, v_e's, and $\bar{v}_e$'s.) In order to update these quantities, thermodynamic quantities such as the pressure are required. In order to calculate these quantities, EVH-1 calculates tables of state variables and interpolates within these tables. The three-dimensional tables are constructed in such a way that ρ, T, and Y_e are the independent variables, and tables are constructed for ϵ, pressure (P), entropy (s), and other variables. For the combination ρ, T, and Y_e in a given zone of our two-dimensional grid, the code performs linear interpolations using the logarithms of both the independent (e.g., ρ) and the dependent (e.g., P) variables in our table to obtain the corresponding dependent variables for that zone. For details of the interpolation scheme, see Mezzacappa & Bruenn (1993).

Because the hydrodynamics evolution updates ρ, ϵ, and Y_e, it is necessary to update T by iteration of

$$\Delta T = \frac{\epsilon^{\mathrm{hyd}} - \epsilon^{\mathrm{int}}}{(\partial \epsilon / \partial T)_{\rho, Y_e}}, \qquad (2)$$

where ϵ^{hyd} and ϵ^{int} are the specific internal energy (1) partially updated by the hydrodynamics and (2) given by the interpolation, respectively, and $(\partial \epsilon / \partial T)_{\rho, Y_e}$ is the specific heat; ϵ^{int} and $(\partial \epsilon / \partial T)_{\rho, Y_e}$ are evaluated at the current iterate, T^0. The iterations occur until ΔT falls below a specified tolerance.

The sweep proceeds by first calling the interpolation routine to update T, and then calculates variables such as P and s in each zone of a one-dimensional sweep. Next, the sweep proceeds by calling the PPM routines for the hydrodynamics evolution, partially updating, ρ, ϵ, and Y_e. Then, the simulations make use of the MGFLD neutrino data in an operator split manner to fully update ϵ and Y_e according to the prescriptions below. The next sweep repeats this procedure, first updating T, then evolving the hydrodynamics, and further updating ϵ and Y_e because of neutrino emission and absorption.

In simulations B, D, F, and L, the neutrino heating and cooling and the change in the electron fraction were computed at each time step within each angular sweep (i.e., at a

given radius) using the following formulae:

$$\frac{\partial \epsilon}{\partial t} = c \sum_{i=1}^{2} \int \frac{E_v^3 \, dE_v [\psi_i^0 / \lambda_i^{(a)} - j_i(1 - \psi_i^0)]}{\rho(hc)^3}, \qquad (3)$$

and

$$\frac{\partial Y_e}{\partial t} = cm_B \sum_{i=1}^{2} \alpha_i \int \frac{E_v^2 \, dE_v [\psi_i^0 / \lambda_i^{(a)} - j_i(1 - \psi_i^0)]}{\rho(hc)^3}, \qquad (4)$$

where E_v, ψ_i^0, $\lambda_i^{(a)}$, and j_i are the electron neutrino or antineutrino energy, zeroth distribution function moment, absorption mean free path, and emissivity, respectively; m_B is the baryon mass; $i = 1$, $\alpha_1 = 1$ corresponds to electron neutrinos, and $i = 2$, $\alpha_2 = -1$ corresponds to electron antineutrinos. As mentioned earlier, the time-dependent ψ_i^0 are obtained from tables in r, t, and E_v constructed from our one-dimensional MGFLD simulations.

Simulations E and H made use of modified versions of the above formulae to account for the "finite time" required for transport of neutrinos between an element of convecting material and its background. The corrected heating rate is calculated from the above heating rate by considering the mean free paths and by calculating a minimum transport time, which is then used to calculate a correction factor. The mean free path, $\lambda(r, E_v, i)$, is calculated from the emission, absorption, and isoenergetic scattering mean free paths for each radius (r), neutrino energy group (E_v), and neutrino type (i). Once $\lambda(r, E_v, i)$ is determined, the diffusion time, $t_{\mathrm{diff}}(r, E_v, i)$, is calculated by

$$t_{\mathrm{diff}}(r, E_v, i) = \frac{(r_{\mathrm{scale}})^2}{c\lambda(r, E_v, i)}, \qquad (5)$$

where r_{scale} is the length scale of a convecting element. In these calculations, this scale was taken to be 10 km, which is about 1 pressure scale height in the convectively unstable region of the core 10–100 ms after bounce. The free escape time, $t_{\mathrm{esc}}(r, E_v, i)$, represents the minimum transport time of neutrinos from the convecting element, and is given by

$$t_{\mathrm{esc}}(r, E_v, i) = \frac{r_{\mathrm{scale}}}{c}. \qquad (6)$$

The free escape time is a physical limit, and it must be used when $t_{\mathrm{diff}}(r, E_v, i)$ becomes so small, i.e., $\lambda(r, E_v, i)$ becomes

so large, that it would imply that neutrinos are propagating faster than the speed of light. The quantity $t_{trans}(r, E_\nu, i)$ smoothly interpolates between $t_{diff}(r, E_\nu, i)$ [small $\lambda(r, E_\nu, i)$] and $t_{esc}(r, E_\nu, i)$ [large $\lambda(r, E_\nu, i)$], and is given by

$$t_{trans}(r, E_\nu, i) = \{[t_{diff}(r, E_\nu, i)]^2 + [t_{esc}(r, E_\nu, i)]^2\}^{1/2} . \quad (7)$$

This expression tends to weight preferentially the larger of $t_{diff}(r, E_\nu, i)$ and $t_{esc}(r, E_\nu, i)$. Next, from $(\partial\epsilon/\partial t)(r, E_\nu, i)$, which is given by the individual terms in the integrand of equation (3), the heating time, $t_e(r, E_\nu, i)$, is given by

$$t_e(r, E_\nu, i) = \frac{\epsilon(r)}{(\partial\epsilon/\partial t)(r, E_\nu, i)} . \quad (8)$$

The correction factor, c_{trans}, is then

$$c_{trans}(r, E_\nu, i) = \frac{t_e(r, E_\nu, i)}{t_e(r, E_\nu, i) + t_{trans}(r, E_\nu, i)} , \quad (9)$$

and the corrected heating rate becomes

$$\left(\frac{\partial\epsilon}{\partial t}\right)_{corrected} = c_{trans}(r, E_\nu, i) \frac{\partial\epsilon}{\partial t} . \quad (10)$$

A correction for the depletonization rate is computed and applied in an analogous manner.

2.3. Initial Conditions

Table 2 contains the initial conditions for our simulations. The unstable region in the 25 $M_\odot$ model, from which our 25 $M_\odot$ simulations are initiated, extended from an enclosed mass of 0.82 $M_\odot$ to an enclosed mass of 1.02 $M_\odot$ for the case in which the prior evolution was calculated with comprehensive neutrino transport. For the low-test case, the region extended from an enclosed mass of 0.97 $M_\odot$ to an enclosed mass of 1.21 $M_\odot$. For the 15 $M_\odot$ model, from which our 15 $M_\odot$ simulations are initiated, the unstable region extended from an enclosed mass of 0.79 $M_\odot$ to an enclosed mass of 1.03 $M_\odot$.

3. RESULTS

In Figure 1 we plot the initial entropy and electron fraction gradients for our 15 and 25 $M_\odot$ models. In the 25 $M_\odot$ case, we plot the gradients for both our original and low-test runs. Note that in the latter case there is a significantly larger initial entropy gradient. Low-test transport during core collapse leads to less deleptonization and, consequently, to a larger inner homologously collapsing core. As a result, at bounce a stronger shock forms (from a larger rebounding inner piston), and it forms farther out in radius. All are evident in the figure. For our original 25 $M_\odot$ model, the neutrinospheres are initially located at (a) 71 km, (b) 63 km, and (c) 73 km for (a) electron neutrinos, (b) electron antineutrinos, and (c) muon and tau neutrinos and antineutrinos. For our low-test runs, the neutrinospheres are initially located at (a) 117 km, (b) 110 km, and (c) 119 km for (a) electron neutrinos, (b) electron antineutrinos, and (c) muon and tau neutrinos and antineutrinos. For our 15 $M_\odot$ model, the neutrinospheres are initially located at (a) 68 km, (b) 59 km, and (c) 69 km for (a) electron neutrinos, (b) electron antineutrinos, and (c) muon and tau neutrinos and antineutrinos.

As a check that our inner and outer running boundary conditions and our procedure for computing the neutrino cooling, heating, and matter deleptonization rates are sufficient to ensure that one-dimensional EVH-1 simulations between the inner and outer boundaries closely match the original MGFLD simulations, in Figures 2a and 2b we plot a comparison of the density, entropy, electron fraction, and velocity profiles for the one-dimensional simulation, B, and the corresponding MGFLD simulation. These two simulations were initiated from the same model and then run independently thereafter (except, of course, that simulation B uses the neutrino and boundary data generated by the MGFLD run). The comparison is made at 71 ms after bounce. Modulo differences at the shock, the agreement between the two simulations is excellent. Differences are expected at the shock because the PPM Godunov-type scheme is better able to resolve it than second-order artificial viscosity methods.

In Figure 3a (Plate 35) we include three two-dimensional entropy slices spanning the first 20 ms of our simulation C, which is a "hydrodynamics-only" model. The development of proto–neutron star convection in the innermost region

TABLE 2

RADIAL RANGES AND ENTROPY AND ELECTRON FRACTION MAXIMA AND MINIMA
FOR OUR INITIAL LEDOUX-UNSTABLE REGIONS

| SIMULATION	SEEDING RADII (km)		ENTROPY $(s = S/kN_B)$		ELECTRON FRACTION	
	r_{min}	r_{max}	s_{min}	s_{max}	$(Y_e)_{min}$	$(Y_e)_{max}$
25 $M_\odot$ Models						
A	33.8	52.0	5.08	6.24	0.118	0.221
B	33.8	52.0	5.08	6.24	0.118	0.221
C	33.8	52.0	5.08	6.24	0.118	0.221
D	33.8	52.0	5.08	6.24	0.118	0.221
E	33.8	52.0	5.08	6.24	0.118	0.221
F	55.4	122.2	3.33	7.74	0.213	0.463
G	55.4	122.2	3.33	7.74	0.213	0.463
H	55.4	122.2	3.33	7.74	0.213	0.463
15 $M_\odot$ Models						
I	31.0	54.2	5.25	6.19	0.116	0.234
J	31.0	54.2	5.25	6.19	0.116	0.234
K	31.0	54.2	5.25	6.19	0.116	0.234
L	31.0	54.2	5.25	6.19	0.116	0.234
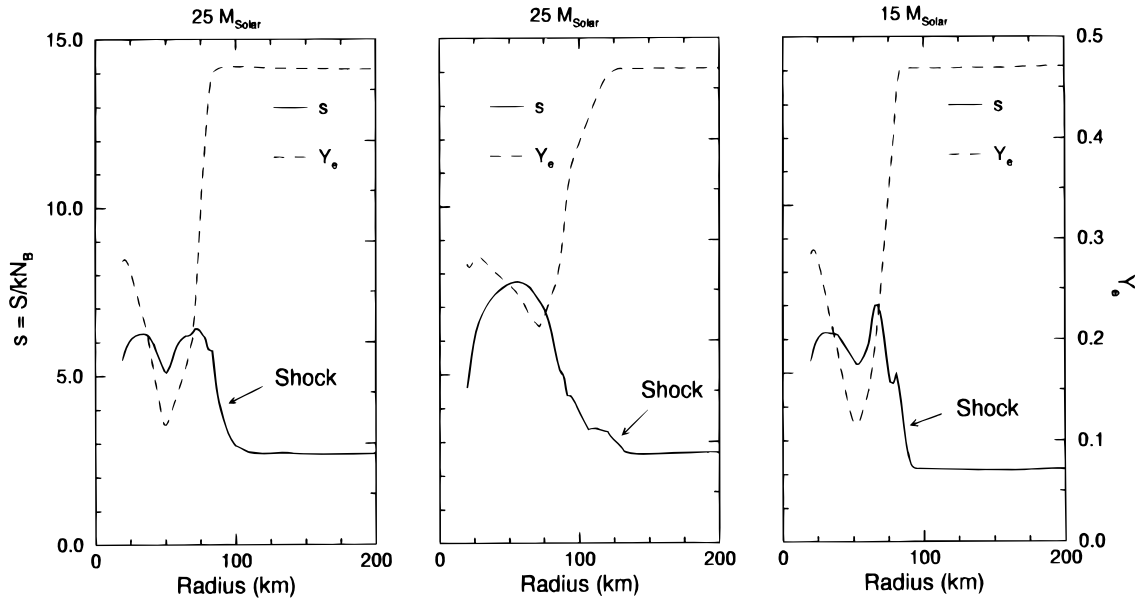
FIG. 1.—Initial entropy and electron fraction profiles for the 25 $M_\odot$, 25 $M_\odot$ "low-test," and 15 $M_\odot$ simulations

below the neutrinospheres (34–52 km) is evident. In the absence of neutrino transport, the redistribution of entropy and electron fraction by convection stabilizes this region, and convection dies out by $t_{pb} = 28$ ms. The redistribution of the entropy and electron fraction profiles by convection is shown in Figure 3c, where we plot the angle-averaged entropy and electron fraction versus radius at the same three time slices shown in Figure 3a. These quantities are defined as follows:

$$\langle S \rangle(i) = \frac{1}{A(i)} \sum_{j=1}^{n_\theta} A(i, j) S(i, j) \tag{11}$$

and

$$\langle Y_e \rangle(i) = \frac{1}{A(i)} \sum_{j=1}^{n_\theta} A(i, j) Y_e(i, j) , \tag{12}$$

where

$$A(i, j) = 2\pi r^2(i) \sin \theta(j) d\theta \tag{13}$$

and where $A(i) = 4\pi r^2(i)$ and $d\theta = \pi/128$. In equations (11) and (12), $S(i, j)$ and $Y_e(i, j)$ are our two-dimensional entropy and electron fraction configurations; the index i runs over $n_r = 128$ radial zones, and the index j runs over $n_\theta = 128$ angles. As $\theta \to 0$, the area of the strip on the 2-sphere spanned by $d\theta$, $A(i, j)$, approaches zero. The angle averaging in equations (11) and (12) is therefore designed to ensure that the averaged quantities near the poles contribute less. In Figure 3c it is seen that, at $t_{pb} = 13$ ms, both entropy and electron fraction gradients are negative below 40 km, but by $t_{pb} = 18$ ms, the entropy gradient has become positive and is tending to stabilize the still negative gradient in electron fraction.

The additional entropy gradients in Figure 3c (e.g., at 100 km) that appear below the shock with time result from the successive strengthening and weakening of the shock as it first propagates out after bounce and as the inner core oscillates in quasi-hydrostatic equilibrium. These gradients give rise to additional Ledoux-unstable regions, and convection develops in these regions, seeded by the initial convection

episode. This is evident in Figure 3a, at $t_{pb} = 28$ ms. The shock is clearly outlined by the large jump in entropy across it. The distortions in the shock's sphericity, when proto–neutron star convection reaches it, are also evident.

In Figure 3b, we plot the angle-averaged radial and angular convection velocities, defined by

$$\langle v_c \rangle_r = \frac{1}{A(i)} \sum_{j=1}^{n_\theta} A(i, j) | | v_r(i, j) | - \langle v \rangle | \tag{14}$$

and

$$\langle v_c \rangle_\theta = \frac{1}{A(i)} \sum_{j=1}^{n_\theta} A(i, j) | v_\theta(i, j) | , \tag{15}$$

where

$$\langle v \rangle = \frac{1}{A(i)} \sum_{j=1}^{n_\theta} A(i, j) | v_r(i, j) | . \tag{16}$$

Within 10 ms, the radial convection velocity in the innermost region peaks between 3.7 and 5.0×10^8 cm^{-1}, whereas the angular convection velocity peaks at a somewhat larger value of 6.2×10^8 cm s^{-1}. The radial convection velocity below the shock reaches a peak value of 10^9 cm s^{-1} after about 20 ms; by then, the angular convection velocity has decreased. Note the anticorrelation between the radial and angular convection velocities. The peaks in the radial velocity correspond to troughs in the angular velocity, and vice versa, which is characteristic of convective "rollover."

In Figure 4a (Plate 36), we include three entropy slices spanning 21 ms in our simulation D. With the inclusion of neutrino transport, there is no evidence of proto–neutron star convection. Providing more quantitative detail, Figure 4b shows that the angle-averaged radial and angular convection velocities peak at values that are orders of magnitude smaller than in simulation C. In the next section, we will present a simple analytical model that illustrates why this occurs.

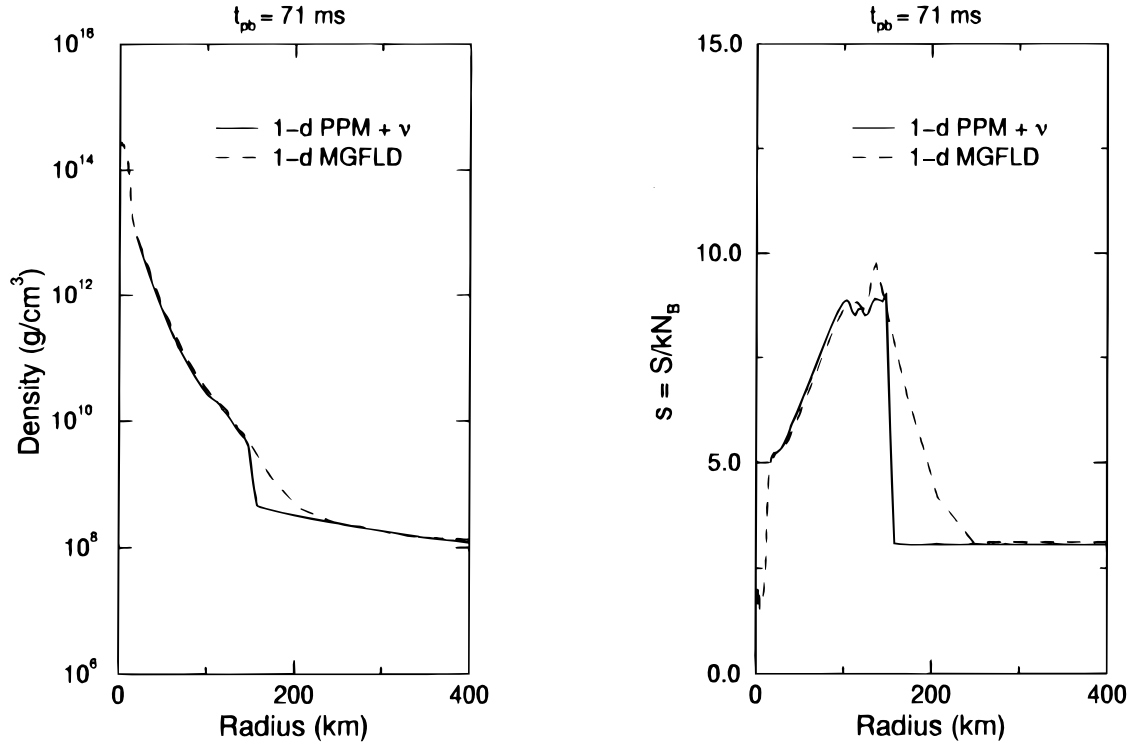Very important to the analysis we will present here and in the next section, and to the overall conclusions of this
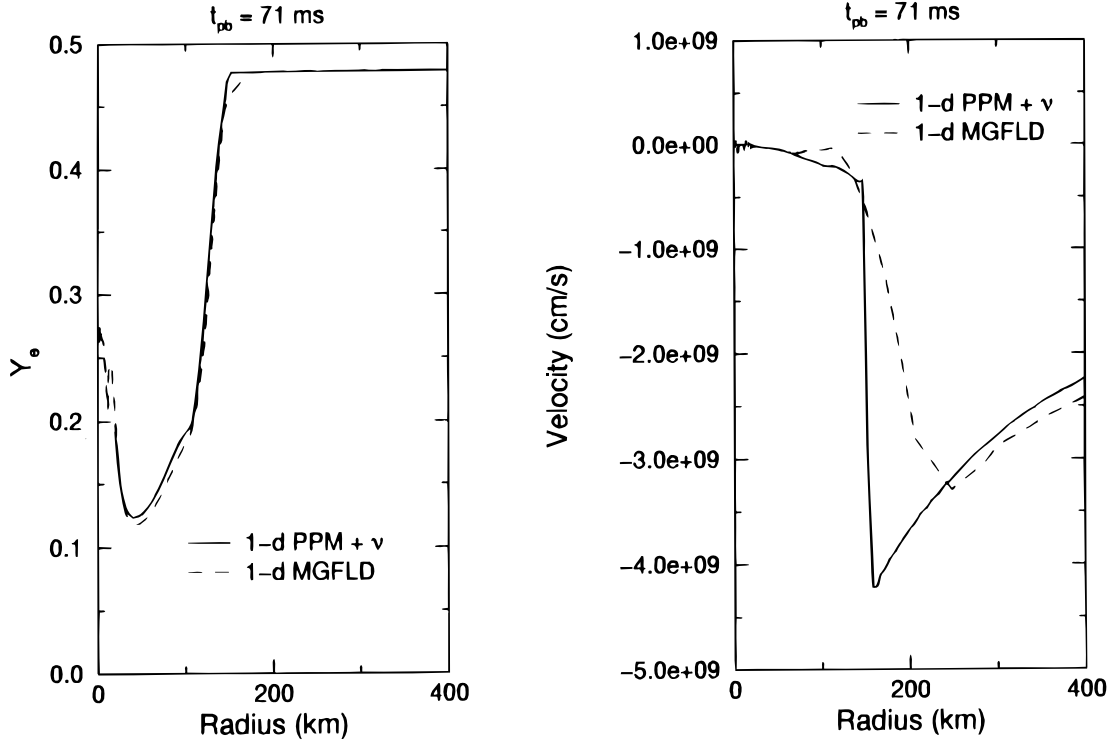
FIG. 2*a*

FIG. 2*b*

FIG. 2.—(*a*) Plot of density and entropy v. radius, comparing a simulation with one-dimensional PPM hydrodynamics and MGFLD neutrino transport (EVH-1; simulation B) to a simulation with one-dimensional Lagrangian hydrodynamics and MGFLD neutrino transport (Bruenn's code). The comparison is made 62 ms into the run. (*b*) Plot of electron fraction and radial velocity v. radius for the same comparison shown in (*a*). (*c*) Plots of the density and entropy profiles at $t_{pb} = 71$ ms, for three different radial grid resolutions in our one-dimensional PPM simulations. (*d*) Plots of the electron fraction and radial velocity profiles at $t_{pb} = 71$ ms, for three different radial grid resolutions in our one-dimensional PPM simulations.
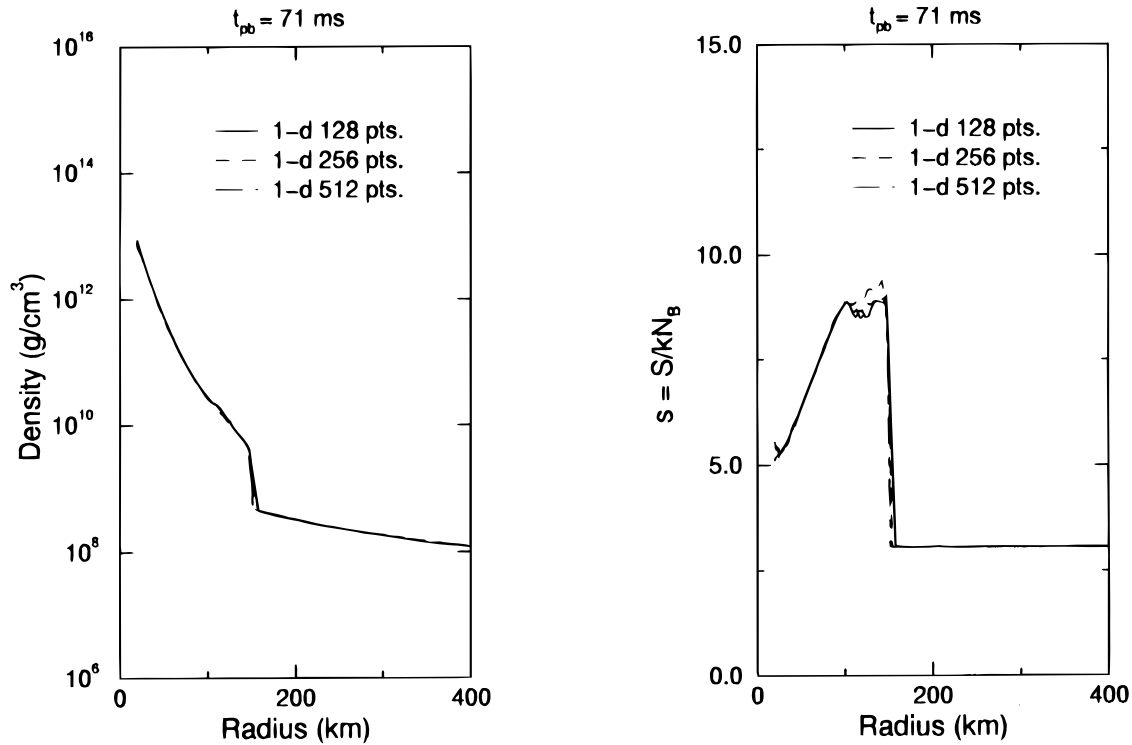
FIG. 2c
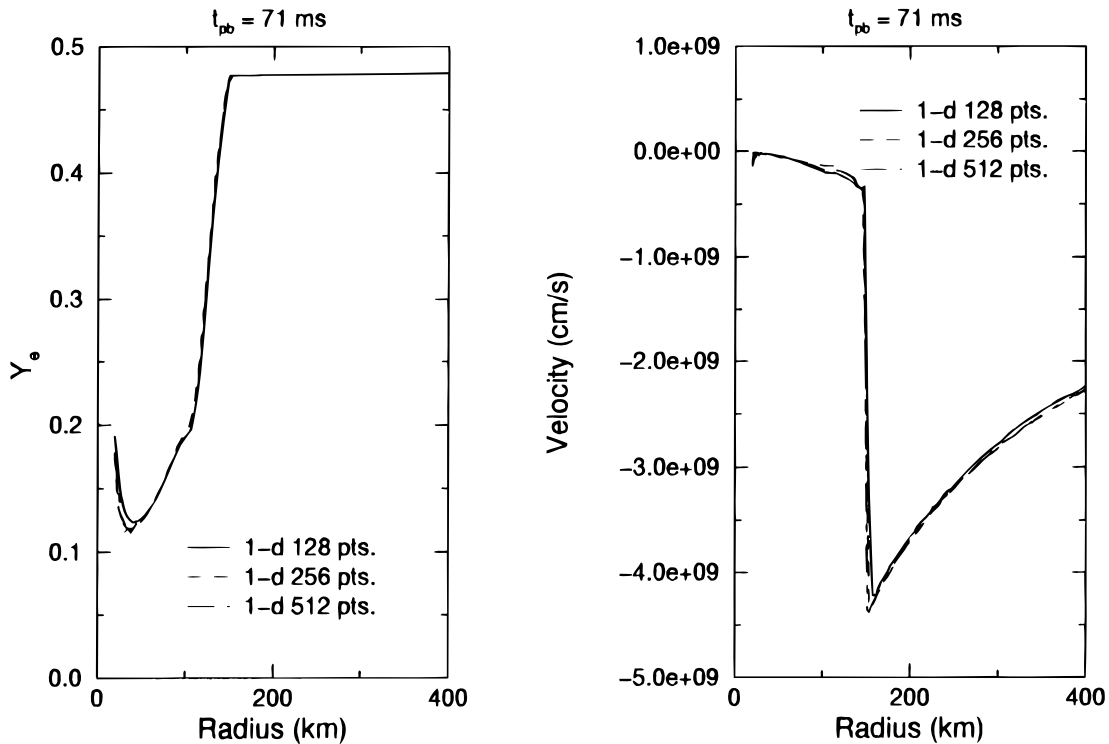
FIG. 2d

paper, is the angle-averaged radial fluid velocity (as opposed to the angle-averaged convection velocities). In Figure 4d (Plate 37) we plot the fluid velocity as a function of radius, early in simulations D and L, with a focus on the innermost 100 km, where proto–neutron star convection first develops in both simulations. Most important to note is that in simulation C, the convection velocities in this region are comparable to the fluid velocity; consequently,

the convective transport of entropy and leptons is evident in Figure 3a. On the other hand, we see that the convection velocities in simulation D are orders of magnitude smaller than the fluid velocity, which explains why convective transport of entropy and leptons is not evident in Figure 4a.

In addition to the effect on the convection velocities, Figure 4c demonstrates transport's effect on the innermost entropy gradient in the initial Ledoux-unstable region. In

this case, the entropy gradient is smoothed out by neutrino diffusion (see also Burrows et al. 1995), whereas in simulation C it was smoothed out by convection. Moreover, Figure 4c shows that the initial lepton gradient is more or less maintained by the same neutrino diffusion. More important, despite the maintenance of this gradient, we see no evidence of proto–neutron star convection over the entire 100 ms spanned by our simulation, counter to what was seen by Burrows (1987), Burrows & Fryxell (1993), Burrows et al. (1995), Janka & Müller (1993b, 1995, 1996), and Keil et al. (1996).

In a self-consistent multidimensional simulation with both multidimensional neutrino transport and hydrodynamics, matter irregularities would give rise to irregularities in the neutrino radiation fields. These would be smoothed out by neutrino transport, which in turn, coming full circle, would smooth out the original matter irregularities. The irregularities in the radiation fields would be smoothed out on transport timescales, which we neglect by imposing already spherically symmetric neutrino distributions. To correct for this, in simulation E we take into account the time it takes for entropy and lepton transport to occur between a convecting fluid element and its surroundings, by modifying the entropy and lepton equilibration rates. This is done as outlined in the previous section. Of course, in a fully self-consistent simulation, the smoothed radiation field may ultimately be different from the spherically symmetric fields we impose. This is a shortcoming of our approximation that we cannot correct. However, we find that transport suppresses proto–neutron star convection significantly, and in so doing, tends to keep the matter spherically symmetric, which in turn would keep the radiation fields close to our imposed fields.

Figure 5a (Plate 38) includes three entropy slices spanning 20 ms in simulation E. Again, as in simulation D, where "finite-time" effects were not considered, there is no evidence of proto–neutron star convection. More quantitatively, Figure 5b illustrates that the peak angle-averaged radial and angular convection velocities are almost an order of magnitude larger than they are in simulation D, but still roughly 2 orders of magnitude smaller than they are in simulation C (a hydrodynamics-only model). Therefore, our conclusion that neutrino transport renders proto–neutron star convection insignificant is not changed. Figure 5c shows once again the smoothing of the innermost entropy gradient and the maintenance of the lepton gradient by neutrino diffusion during the course of the simulation.

To further enhance proto–neutron star convection's chances of developing in the presence of neutrino transport, and to further explore the interplay between neutrino transport and proto–neutron star convection, we have carried out several runs with low-test initial conditions, in which the initial entropy gradient, which initially drives proto–neutron star convection, is maximized. Figure 6a (Plate 39) includes three entropy slices from simulation F, in which neutrino transport is turned off. The large initial entropy gradient is evident in the first slice, and proto–neutron star convection develops rather dramatically within 10 ms after the start of our run. After an additional 10 ms (at $t_{\rm pb} = 27$ ms), convection has reached the shock and has distorted it significantly. Figure 6b shows the peak angle-averaged radial and angular convection velocities. At $t_{\rm pb} \sim 16$ ms, the peak convection velocities for simulations C and F are comparable, but by $t_{\rm pb} \sim 26$ ms, the velocities in the innermost

region in simulation F are roughly 2 times larger, and the outer peak in radial convection velocity is still developing, indicating that the convection growth time for simulation F is longer. Figure 6c shows the rather dramatic and rapid smoothing of the initial entropy and lepton fraction gradients below ~ 100 km that occurs in this simulation.

In Figure 7a (Plate 40), the three entropy slices show minimal proto–neutron star convection developing within 10 ms of the start of simulation G, which includes neutrino transport, but begins with the same low-test initial conditions used in simulation F. However, by $t_{\rm pb} = 27$ ms, at least in the two-dimensional entropy plot, the configuration appears once again to be spherically symmetric. Examination of the convection velocities in Figure 7b shows that, relative to simulation F, the velocities are reduced, particularly at $t_{\rm pb} = 27$ ms, where they are significantly reduced. Figure 7c shows the smoothing of the entropy gradient in the initial Ledoux-unstable region and the maintenance of the lepton gradient that is consistently exhibited by all of our two-dimensional simulations that include neutrino transport (simulations D, E, G, and H).

To help proto–neutron star convection even more, we carried out simulation H, which uses the low-test initial conditions used in simulations F and G, and the reduced entropy and lepton equilibration rates used in simulation E. Figure 8a (Plate 41) shows three entropy slices from this simulation. Again, at $t_{\rm pb} = 17$ ms, minimal proto–neutron star convection is evident, but after an additional 10 ms, the two-dimensional entropy configuration appears to be spherically symmetric. A look at Figure 8b shows that the peak radial and angular convection velocities are 5–10 times smaller relative to their values in simulation F (low-test initial conditions, hydrodynamics-only model). Figure 8c shows the evolution in the entropy and electron fraction gradients, with the expected smoothing of the initial entropy gradient during the first 20 ms by neutrino diffusion, and the maintenance of the lepton gradient.

Figure 9 (Plate 42) illustrates the long-term behavior in entropy in simulations D, E, and G. No convection is evident in simulation D at 86 ms into our run, and minimal convection is evident in simulation E at about the same time. In contrast, in the low-test simulation, G, more vigorous proto–neutron star convection has developed at this later time in our run than appeared at earlier times (see Fig. 7a).

Figures 10a–10c (Plate 43) and 11a–11c (Plate 44) depict the evolution in entropy, convection velocities, and entropy and electron fraction gradients for our 15 $M_\odot$ model. The same behavior exhibited by the 25 $M_\odot$ model is exhibited here, indicating that our conclusions regarding neutrino transport's tendency to inhibit the development of proto–neutron star convection are independent of stellar mass and the size and profile of the initial precollapse or postbounce cores.

4. ANALYTIC MODEL

Convection near or below the neutrinospheres can be profoundly influenced by the neutrino transport of energy and leptons between a convecting fluid element and the background. In effect, convection becomes "leaky," and differences between a convecting fluid element's entropy and lepton fraction and the background's entropy and lepton fraction, for which the buoyancy force driving convection arises, are reduced. To construct the simplest model of this,

we will assume that the lepton fraction gradient is zero and that convection is driven by a negative entropy gradient that is constant in space and time. (Reversing the roles of the entropy and lepton fraction gradients would give analogous results. The more general case in which both gradients are nonzero has been considered by Bruenn & Dineva 1996. This complicates the analysis and can lead to additional modes of instability, such as semiconvection and neutron fingers, which are not relevant here.) We will also assume that the effect of neutrino transport is to equilibrate the entropy of a fluid element with the background entropy in a characteristic timescale, τ_s.[7] If the fluid element and the background are in pressure balance, and if we neglect viscosity (microscopic and turbulent) and keep only first-order terms, the fluid element's equations of motion are

$$\dot{v} = \frac{g}{\rho} \, \alpha_s \theta_s \tag{17}$$

and

$$\dot{\theta}_s = -\frac{\theta_s}{\tau_s} - \frac{d\bar{s}}{dr} \, v \ . \tag{18}$$

where $\theta_s = s - \bar{s}$, with s and $\bar{s}$ being the fluid element's entropy and the background's entropy, respectively; g is the local acceleration of gravity; v is the radial velocity; and $\alpha_s \equiv -(\partial \rho / \partial s)_{P, Y_\ell} > 0$, where Y_ℓ is the common lepton fraction. Equation (17) equates the fluid element's acceleration to the buoyancy force arising from the difference between its entropy and the background's entropy; equation (18) equates $\dot{\theta}_s$ to $\dot{s}$ minus $\dot{\bar{s}}$, where $\dot{s}$ results from the fluid element's equilibration with the background, and $\dot{\bar{s}}$ results from its motion through the gradient in $\bar{s}$.

If we neglect neutrino effects ($\tau_s = \infty$), the solutions to equations (17) and (18) indicate that (1) if $d\bar{s}/dr > 0$, the fluid element oscillates with the Brunt-Väisälä frequency $\omega_{\mathrm{BV}_s} \equiv [(g\alpha_s \, d\bar{s}/dr)/\rho]^{1/2}$, and (2) if $d\bar{s}/dr < 0$, it convects, i.e., its velocity increases exponentially, and the convection growth timescale is given by $\tau = \tau_{\mathrm{BV}_s} \equiv [-(g\alpha_s \, d\bar{s}/dr)/\rho]^{-1/2}$. When neutrino transport effects are included in the convectively unstable case ($d\bar{s}/dr < 0$), the fluid element convects, but the convection growth timescale $\tau > \tau_{\mathrm{BV}_s}$ is given by $1/\tau = [1/\tau_{\mathrm{BV}_s}^2 + 1/4\tau_s^2]^{1/2} - 1/2\tau_s$. In the limit $\tau_s \ll \tau_{\mathrm{BV}_s}$, the growth timescale increases by $\tau_{\mathrm{BV}_s}/\tau_s$, i.e., $\tau \simeq \tau_{\mathrm{BV}_s}^2/\tau_s$.

In addition to reducing convection's growth rate, neutrino transport also reduces its asymptotic velocities. In particular, in the limit $\tau_s \ll \tau_{\mathrm{BV}_s}$, the solutions to equations (17) and (18) show that a fluid element's velocity after moving a distance ℓ from rest is reduced by the factor $\tau_s/\tau_{\mathrm{BV}_s}$.

To apply this analysis to proto–neutron star convection, we note that $\tau_{\mathrm{BV}_s} = 1.8$ ms at the neutrinosphere ($\rho \sim 3 \times 10^{11}$ g cm^{-3}) and 1.4 ms at 10^{12} g cm^{-3}. These values are representative of both models, S15s7b and

S25s7b, after bounce, and are computed for a typical postbounce s gradient of 1 in 30 km, and no gradient in Y_ℓ. Similarly, $\tau_{\mathrm{BV}_s} = 12.3$ ms at the neutrinosphere and 16.6 ms at 10^{12} g/cm^{-3}. These values are computed for a postbounce gradient of 0.1 in 30 km, and no gradient in s. On the other hand, our $\dot{\epsilon}$ from neutrino heating and cooling, including finite-time corrections, gives values for τ_s that decrease from 0.62 ms at the neutrinosphere to 0.03 ms at 10^{12} g cm^{-3}, for our 25 $M_\odot$ model, and from 0.65 ms at the neutrinosphere to 0.028 ms at 10^{12} g cm^{-3}, for our 15 $M_\odot$ model. Note that the numbers are fairly independent of the precollapse model. Our $\dot{Y}_e$, with finite-time corrections, gives lepton equilibration times of 0.049 ms at the neutrinosphere and 0.018 ms at 10^{12} g cm^{-3}, for our 25 $M_\odot$ model, and 0.054 ms at the neutrinosphere and 0.017 ms at 10^{12} g cm^{-3}, for our 15 $M_\odot$ model. These imply that neutrino transport should reduce the growth rate and asymptotic velocities of entropy-driven (lepton-driven) convection by a factor ~ 3 (50) at the neutrinosphere and a factor ~ 250 (1000) at 10^{12} g cm^{-3}, for both the 15 and 25 $M_\odot$ models. Our simulations are consistent with these results.

5. SUMMARY, DISCUSSION, AND CONCLUSIONS

In the absence of neutrino transport, for both our 15 and 25 $M_\odot$ models the angle-averaged radial and angular convection velocities in the initial Ledoux-unstable region below the shock after bounce achieve their peak values in ~ 20 ms, after which they decrease as the convection in this region dissipates. The dissipation occurs as the initial postbounce entropy and lepton gradients are smoothed out by convection. The initial proto–neutron star convection episode seeds additional proto–neutron star convection beneath the shock, which is driven by successive entropy gradients that develop above the initially unstable region, as the shock propagates out after core bounce and is in turn strengthened and weakened by the oscillating inner core.

In the presence of neutrino transport, proto–neutron star convection velocities are too small relative to the bulk inflow velocities to result in any significant convective transport of entropy and leptons. Our two-dimensional entropy profiles remain for all intents and purposes spherically symmetric, and the peak angle-averaged radial and angular convection velocities are orders of magnitude smaller than they are in the corresponding hydrodynamics-only models.

When neutrino transport is included in any of our simulations, the initial postbounce entropy gradient is smoothed out by neutrino diffusion, whereas the initial lepton gradient is maintained by electron capture and neutrino escape near the neutrinosphere. Counter to what was seen by Burrows (1987), Burrows & Fryxell (1993), Burrows et al. (1995), Janka & Müller (1993b, 1995, 1996), and Keil et al. (1996) despite the persistence of the lepton gradient, proto–neutron star convection develops in the 100 ms spanned by our simulations only in our low-test simulation, which begins with unrealistic initial entropy and lepton gradients that result from an unrealistic core-collapse simulation with oversimplified neutrino transport.

We have included simulations in which the entropy and lepton equilibration rates (as defined in § 2) were reduced by considering the neutrino diffusion time across a convecting element of pressure-scale-height size; i.e., by using the largest convecting element, we overestimate the equilibration suppression. Details can be found in § 2. Despite the

---

[7] We realize that temperature is the appropriate thermodynamic variable to describe the equilibration in energy of two systems in thermal contact, as is the chemical potential for equilibration in particle number. Because our system is in nuclear statistical equilibrium, it is legitimate to consider equilibration in terms of the variables s and Y_ℓ; i.e., when the temperatures and chemical potentials of the two systems in pressure balance become equal, their s's and Y_ℓ's are also equal. Using the same variables to describe equilibration that are used to describe convective instability greatly simplifies the picture.

reduction in rates, our conclusions are not altered. The two-dimensional entropy profiles show minimal protoneutron star convection development, and the ratio of the angle-averaged radial and angular convection velocities to their counterparts in the hydrodynamics-only models remain small.

In other simulations, we optimized proto–neutron star convection's chances of developing by starting with low-test initial conditions. These conditions were generated by core-collapse simulations that incorporated low-test neutrino transport, ignoring the important deleptonization effects of neutrino-electron scattering (NES), and the further deleptonization accompanying ion-ion screening corrections to the neutral-current coherent isoenergetic scattering on nuclei, which dominates the neutrino opacity during infall. It is well known that less deleptonization occurs when NES is neglected, resulting in a larger inner core, a stronger initial shock, a larger initial shock radius, and a larger initial entropy gradient that will subsequently drive a more vigorous proto–neutron convection. Whereas the initial proto–neutronstar convection episode in the hydrodynamics-only model was rather dramatic, with neutrino transport included the behavior observed in simulations beginning with realistic initial conditions was repeated. The two-dimensional entropy profiles showed very little proto–neutron star convection, and the angle-averaged radial and angular convection velocities were significantly reduced relative to their values in the hydrodynamics-only model. This occurred even in a final simulation in which we provided proto–neutron star convection with its best chance of developing, by starting with low-test initial conditions while simultaneously implementing reduced entropy and lepton equilibration rates to account for neutrino diffusion.

A simple analytic model supports our numerical results, and demonstrates that neutrino transport reduces the convection growth rates and asymptotic velocities by a factor of $\tau_{\mathrm{BV}_s}/\tau_s$, for entropy-driven convection, and by a factor of $\tau_{\mathrm{BV}_{Y_\ell}}/\tau_{Y_\ell}$, for lepton-driven convection, where τ_s and τ_{Y_ℓ} are the timescales for equilibrating via neutrino transport a convecting element with the background, in entropy and leptons, respectively, and $\tau_{\mathrm{BV}_{s,Y_\ell}}$ are the e-folding times for convection's growth in the absence of neutrino transport. With finite-time corrections to the equilibrium rates, the ratio $\tau_{\mathrm{BV}_s}/\tau_s$ ranges from ~ 3 to ~ 250 between the neutrinosphere and 10^{12} g cm^{-3}; the ratio $\tau_{\mathrm{BV}_{Y_\ell}}/\tau_{Y_\ell}$ ranges from ~ 50 to ~ 1000.

Most prior multidimensional simulations of proto–neutron star convection (e.g., Burrows & Fryxell 1992, 1993; Janka & Müller 1993b, 1996) have either ignored neutrino transport entirely or have employed radial-ray neutrino transport. While the latter is necessitated by the extreme computational challenge imposed by true multidimensional transport, it ignores the tendency of neutrino transport to equilibrate upflows and downflows with each other in energy and leptons, thus reducing the very buoyancy contrast driving these flows. Our one-dimensional neutrino transport is complementary to radial-ray transport in this regard. Imposing a spherically symmetric neutrino distribution is equivalent to maximizing the lateral angular transport of neutrinos between ascending high-entropy and descending low-entropy convecting elements, which would be expected to suppress proto–neutron star convection as the rising and falling flows equilibrate in entropy and leptons. No doubt differences between our results and those of the aforementioned groups derive in part from these two very different transport approximations (as well as from our use of multigroup transport and their use of gray transport that in semitransparent regions breaks down).

To assess the validity of our neutrino transport approximation, i.e., our use of precalculated spherically symmetric neutrino distributions, we can compare our equilibration times with those obtained from detailed neutrino equilibration experiments (Bruenn et al. 1995, Bruenn & Dineva 1996, 1997). These are shown in Figure 12. The equilibration timescales, τ_s and τ_{Y_ℓ}, correspond to a perturbation of a fluid element in entropy and lepton fraction, respectively, and both equilibration timescales are computed for a fluid perturbation scale equal to 1 pressure scale height, which is ~ 10 km at all densities. For smaller length scales, the equilibration timescales would be reduced. As defined in
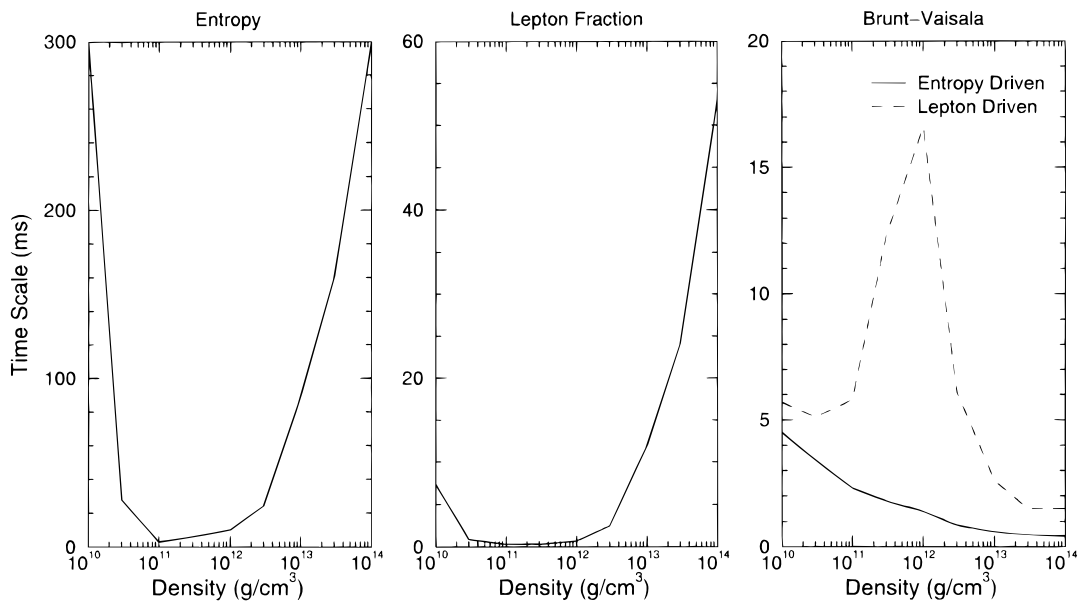

FIG. 12.—Plots showing the entropy and lepton-fraction equilibration timescales, and the convection (Brunt-Väisälä) timescales, as a function of density

§ 4, the Brunt-Väisälä timescale, τ_{BV_s}, is computed for a gradient in s of 1 in 30 km, and no gradient in Y_ℓ, and is appropriate for entropy-driven convection. Similarly, the Brunt-Väisälä timescale, $\tau_{BV_{Y_\ell}}$, is computed for a gradient in Y_ℓ of 0.1 in 30 km, and no gradient in s, and is appropriate for lepton-driven convection. Both τ_s and τ_{Y_ℓ} exhibit a minimum near the neutrinosphere. At higher densities, they increase because of slow neutrino diffusion, and at low densities, they increase because of weak neutrino coupling with the matter.

The equilibration experiments show that a fluid element of 1 pressure scale height in radius will equilibrate in entropy in a minimum time of 3.1 ms, which occurs at $\sim 10^{11}$ g cm^{-3}. Smaller modes will equilibrate faster. The lepton equilibration time has a minimum of 0.29 ms, which also occurs at $\sim 10^{11}$ g cm^{-3}. On the other hand, our $\dot{\epsilon}$ (with finite-time corrections) gives τ_s values for our 25 $M_\odot$ model that decrease from 0.62 ms at the neutrinosphere ($\sim 3 \times 10^{11}$ g cm^{-3}), which is ~ 10 times shorter than is observed in the equilibration experiments, to 0.03 ms at 10^{12} g cm^{-3}, which is ~ 333 times shorter than is observed in the equilibration experiments. Similarly, values for our 15 $M_\odot$ model decrease from 0.65 ms at the neutrinosphere to 0.028 ms at 10^{12} g cm^{-3}. Our $\dot{Y}_e$ (with finite-time corrections) gives τ_{Y_ℓ} values for our 25 $M_\odot$ model that decrease from 0.049 ms at the neutrinosphere, which is ~ 6 times shorter than is observed in the equilibration experiments, to 0.018 ms at 10^{12} g cm^{-3}, which is ~ 38 times shorter than is observed in the equilibration experiments. Similarly, values for our 15 $M_\odot$ model decrease from 0.054 ms at the neutrinosphere to 0.017 ms at 10^{12} g cm^{-3}.

Because the density in the initial Ledoux-unstable region in our 25 $M_\odot$ model ranges from 6.9×10^{11} g cm^{-3} at the top of the region to 1.38×10^{12} g cm^{-3} at the bottom, and in our 15 $M_\odot$ model it ranges from 5.49×10^{11} g cm^{-3} to 1.52×10^{12} g cm^{-3}, at the outset of our simulations we are in a density range in which, based on our timescale analysis, we may seriously overestimate the entropy and lepton equilibration rates, even with finite-time corrections. Whether or not we must revise our conclusions regarding the effect of neutrino transport on the growth of convection depends, as we discuss below, on the type of proto–neutron star convection.

Entropy-driven or entropy- and lepton-driven convection.—As shown in Figure 12, the ratio of the Brunt-Väisälä timescales to the entropy equilibration timescales given by the equilibration experiments is always greater than unity, implying that the equilibration time is longer than the convection growth time. Therefore, based on this alone, there is no doubt that in our approximation we overestimate transport's effect in suppressing convection.

Lepton-driven convection.—On the other hand, after the unstable entropy gradients have been eliminated by an initial round of entropy-driven convection, or by neutrino diffusion, proto–neutron star convection tends to continue, driven by a negative lepton fraction gradient maintained by ongoing deleptonization at the neutrinosphere. This lepton-driven proto–neutron star convection is forced by lepton fraction differences between convecting fluid elements and the background. The lepton equilibration timescales are given in Figure 12 by τ_{Y_ℓ}. Figure 12 also shows the Brunt-Väisälä timescales, $\tau_{BV_{Y_\ell}}$. The lepton equilibration timescales are significantly smaller than the convection growth times ($\tau_{BV_{Y_\ell}}$) for densities between 3×10^{10} and 3×10^{12} g cm^{-3}; therefore, in the case of lepton-driven convection, which is the most important of proto–neutron star convection modes, our conclusions regarding the tendency of neutrino transport to severely suppress convection are realistic.

In conclusion, there is clearly a need to self-consistently couple multidimensional multigroup realistic neutrino transport and multidimensional hydrodynamics in optically thick regions before we or any other group can draw final conclusions regarding the development of proto–neutron star convection, or any mode of convection below the neutrinospheres, in core-collapse supernovae. Nonetheless, our compendium of results, supported by our analytic model and timescale analyses, is compelling, pointing to a very real effect: Neutrino transport will suppress proto–neutron star convection, the extent of which lies somewhere between what we have computed and what other groups have computed. The question is: Where?

REFERENCES

Arnett, W. D. 1986, in IAU Symp. 125, The Origin and Evolution of Neutron Stars, ed. D. J. Helfand & J. H. Huang (Dordrecht: Reidel), 273
———. 1987, ApJ, 319, 136
Bazan, G., & Arnett, W. D. 1994, ApJ, 433, L41
Bethe, H. A. 1990, Rev. Mod. Phys., 62, 801
———. 1993, ApJ, 412, 192
Bethe, H. A., Brown, G. E., & Cooperstein, J. 1987, ApJ, 322, 201
Bethe, H., & Wilson, J. R. 1985, ApJ, 295, 14
Bruenn, S. W. 1993, in Nuclear Physics in the Universe, ed. M. W. Guidry & M. R. Strayer (Bristol: IOP), 31

Bruenn, S. W. 1985, ApJS, 58, 771
Bruenn, S. W., Buchler, J. R., & Livio, M. 1979, ApJ, 234, L183
Bruenn, S. W., & Dineva, T. 1996, ApJ, 458, L71
———. 1997, in preparation
Bruenn, S. W., & Mezzacappa, A. 1994, ApJ, 433, L45
Bruenn, S. W., Mezzacappa, A., & Dineva, T. 1995, Phys. Rep., 256, 69
Burrows, A. 1987, ApJ, 318, L63
Burrows, A., & Fryxell, B. A. 1992, Science, 258, 430
———. 1993, ApJ, 418, L33
Burrows, A., & Goshy, J. 1993, ApJ, 416, L75
Burrows, A., Hayes, J., & Fryxell, B. A. 1995, ApJ, 450, 830

Burrows, A., & Lattimer, J. M. 1988, Phys. Rep., 163, 5
Colgate, S. A., Herant, M., & Benz, W. 1993, Phys. Rep., 227, 157
Colgate, S. A., & Petschek, A. G. 1980, ApJ, 236, L115
Colgate, S. A., & White, R. H. 1966, ApJ, 143, 626
Cooperstein, J. 1993, in Nuclear Physics in the Universe, ed. M. W. Guidry
    & M. R. Strayer (Bristol: IOP), 99
Epstein, R. I. 1979, MNRAS, 188, 305
Herant, M., Benz, W., & Colgate, S. A. 1992, ApJ, 395, 642
Herant, M., Benz, W., Hix, W. R., Fryer, C. L., & Colgate, S. A. 1994, ApJ,
    435, 339
Janka, H.-Th., & Müller, E. 1993a, in IAU Colloq. 145, Supernovae and
    Supernova Remnants, ed. R. McCray & Wang Zhenru (Cambridge:
    Cambridge Univ. Press), 109
————. 1993b, in Frontiers of Neutrino Astrophysics, ed. Y. Suzuki &
    K. Nakamura (Tokyo: Universal Academy), 203
————. 1995, ApJ, 448, L109
————.1996, A&A, 306, 167
Keil, W., Janka, H.-Th., & Müller, E. 1996, ApJ, 473, L111
Lattimer, J. M., & Mazurek, T. J. 1981, ApJ, 246, 995
Lattimer, J. M., & Swesty, F. D. 1991, Nucl. Phys. A, 535, 331
Livio, M., Buchler, J. R., & Colgate, S. A. 1980, ApJ, 238, L139

Mayle, R. W. 1985, Ph.D. thesis, Univ. California, Berkeley
Mezzacappa, A., & Bruenn, S. W. 1993, ApJ, 405, 669
Mezzacappa, A., Calder, A. C., Bruenn, S. W., Blondin, J. M., Guidry,
    M. W., Strayer, M. R., & Umar, A. S. 1998, ApJ, 495, in press
Miller, D. S., Wilson, J. R., & Mayle, R. W. 1993, ApJ, 415, 278
Müller, E. 1993, in Proc. Seventh Workshop on Nuclear Astrophysics, ed.
    W. Hillebrandt & E. Müller (Garching: Max-Planck-Institut für
    Astrophysik), 27
Müller, E., & Janka, H.-Th. 1994, in Proc. Int. Conf. Ges., Revs. Mod.
    Astron. 75, ed. G. Klure (Hamburg: Astron. Ges.), 103
Shimizu, T., Yamada, S., & Sato, K. 1993, PASJ, 45, L53
————. 1994,ApJ, 432, L119
Smarr, L., Wilson, J. R., Barton, R. T., & Bowers, R. L. 1981, ApJ, 246, 515
Weaver, T. A., & Woosley, S. E. 1998, in preparation
Wilson, J. R. 1985, Numerical Astrophysics, ed. J. M. Centrella et al.
    (Boston: Jones & Bartlett), 422
Wilson, J. R., & Mayle, R. W. 1988, Phys. Rep., 163, 63
————. 1993, Phys. Rep., 227, 97
Wilson, J. R., Mayle, R. W., Woosley, S. E., & Weaver, T. 1986, in Ann. NY
   Acad. Sci., 470, 367
Woosley, S. E., & Weaver, T. A. 1995, ApJS, 101, 181
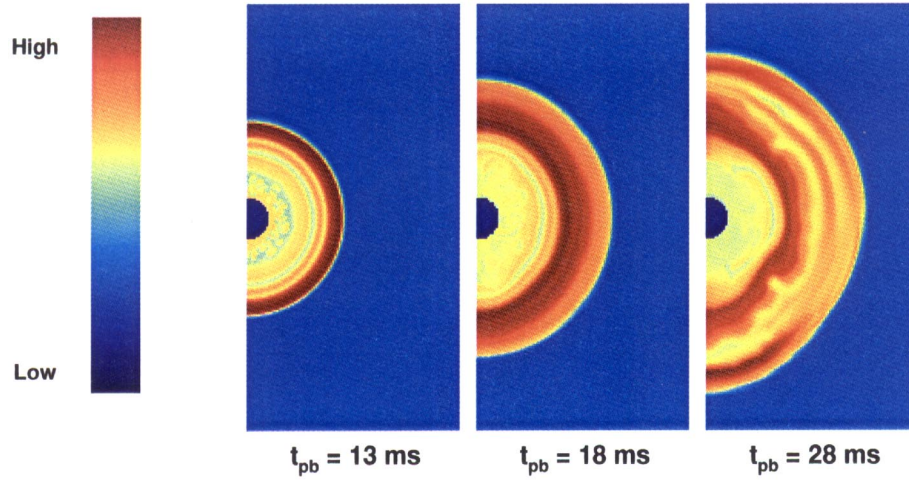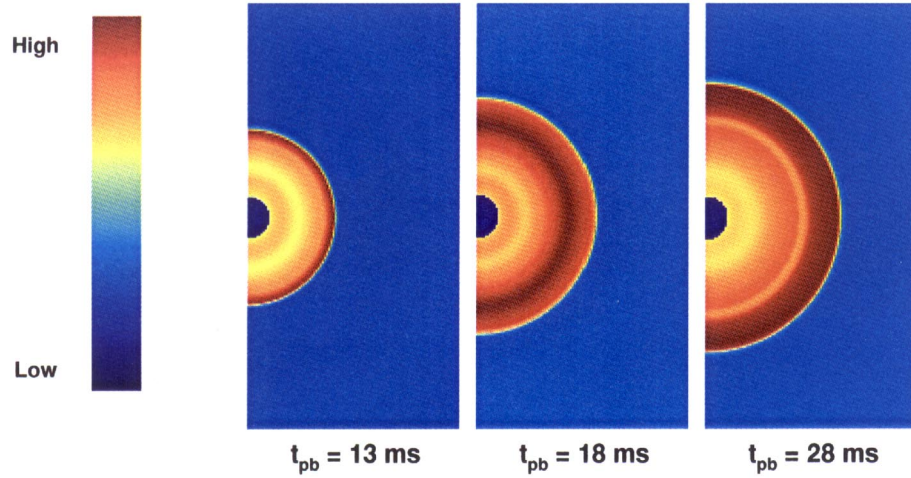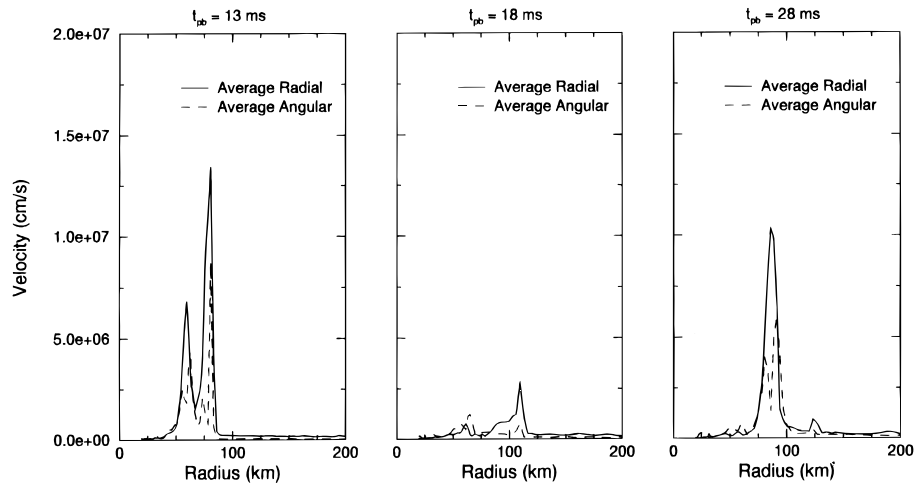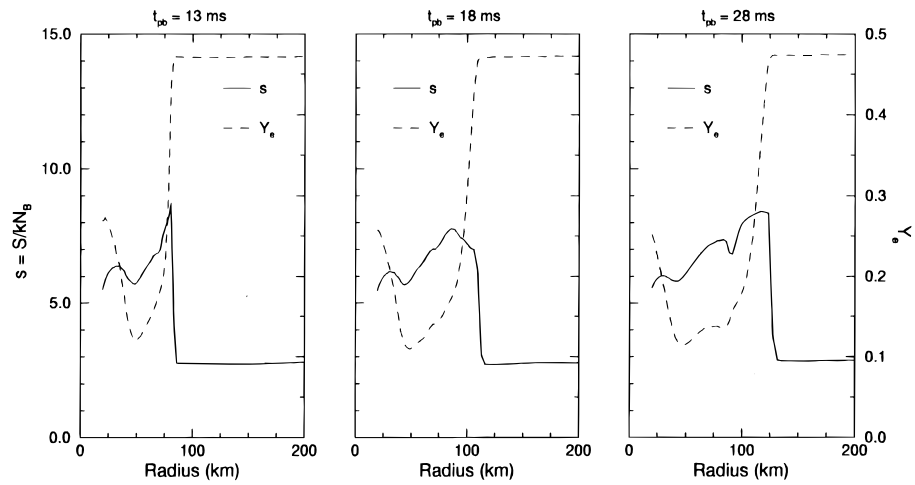
FIG. 3a
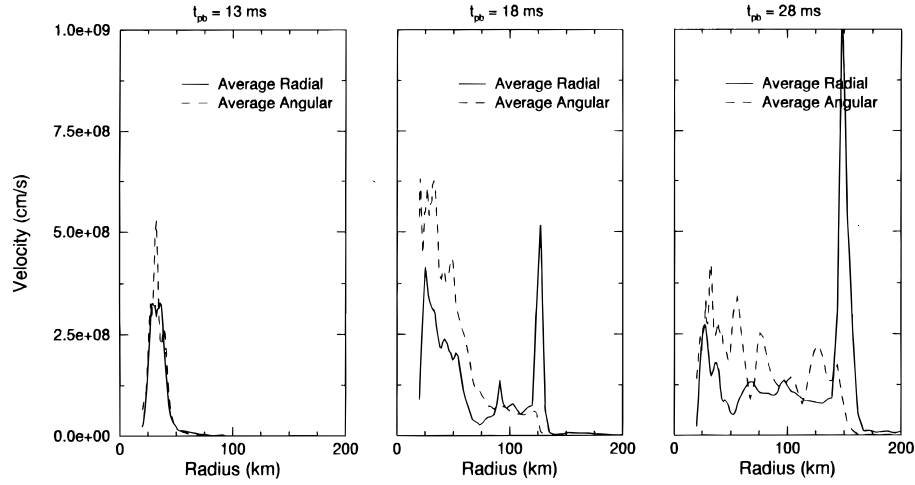
FIG. 3b
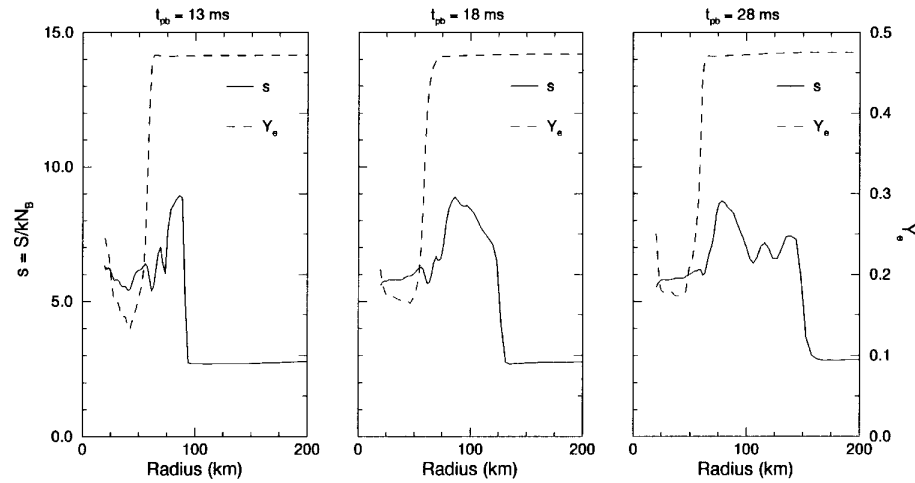
FIG. 3c

FIG. 3.—(a) Two-dimensional plots showing the entropy evolution of the 25 $M_\odot$ model in a simulation without neutrino transport (simulation C). (b) Plots of the angle-averaged radial and angular convection velocities corresponding to the three entropy snapshots in (a). (c) Plots showing the angle-averaged entropy and electron fraction profiles corresponding to the three entropy snapshots in (a).
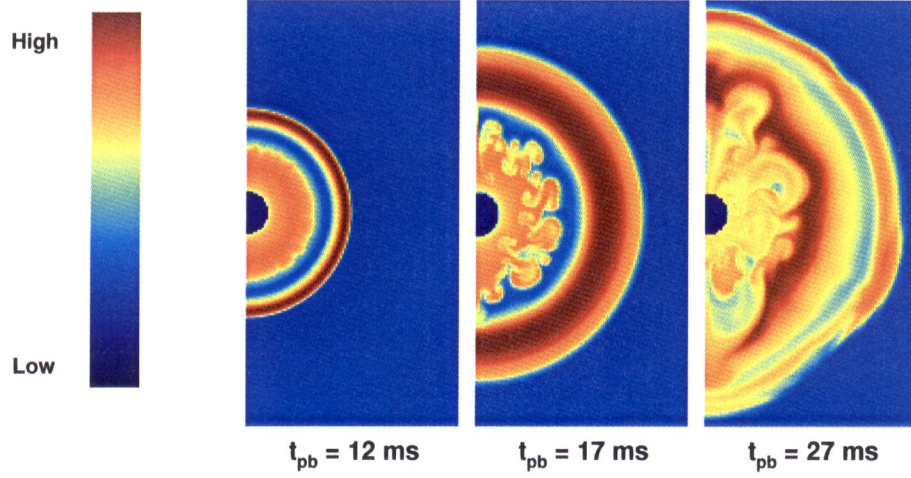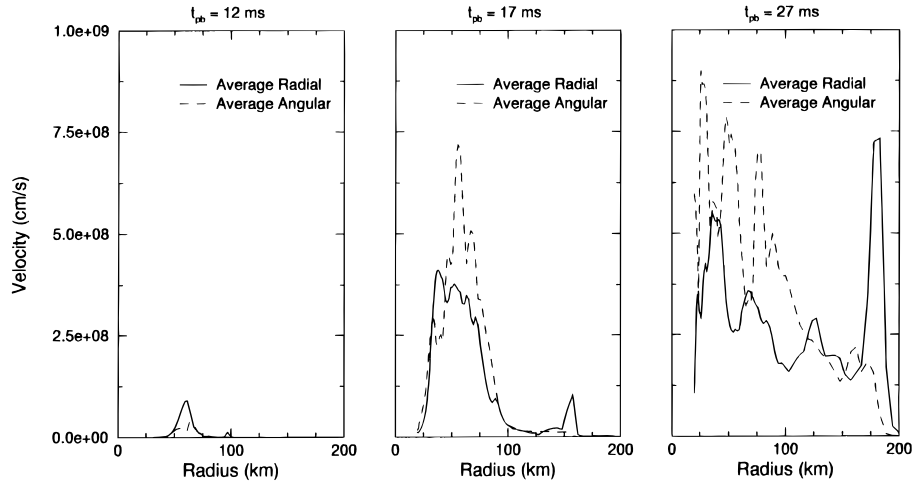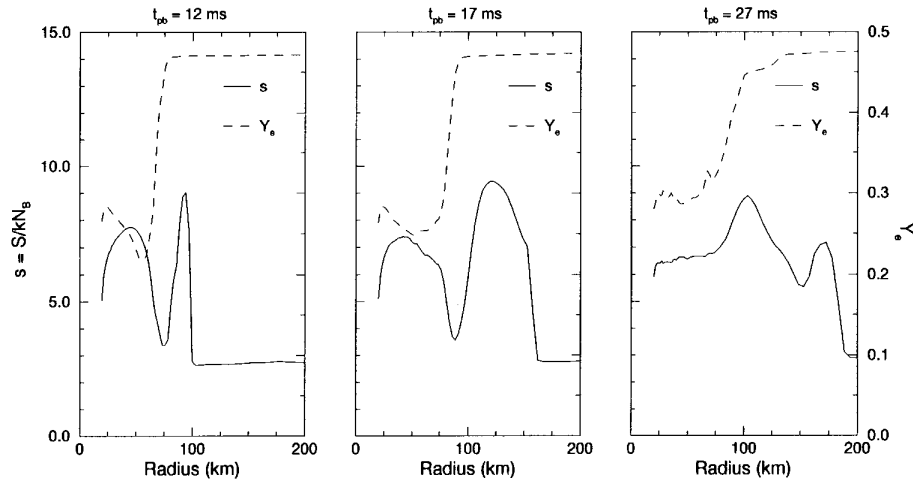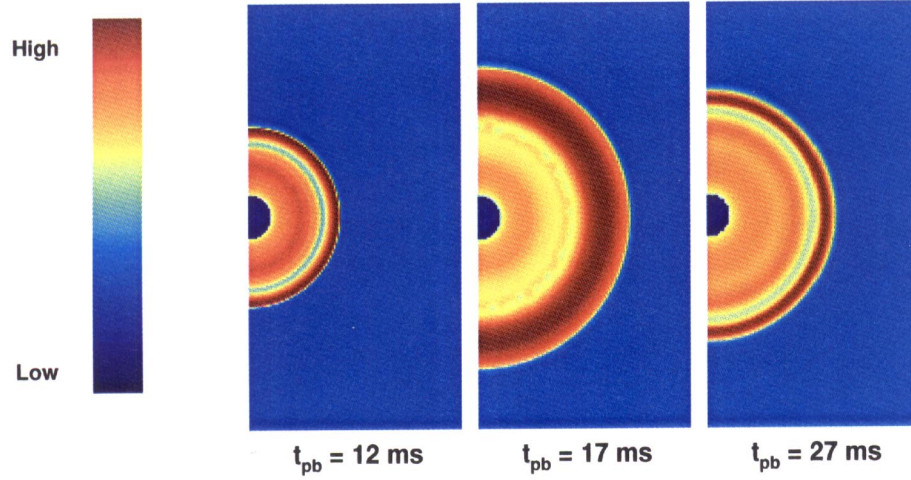
MEZZACAPPA et al. (see 493, 854)

PLATE 35
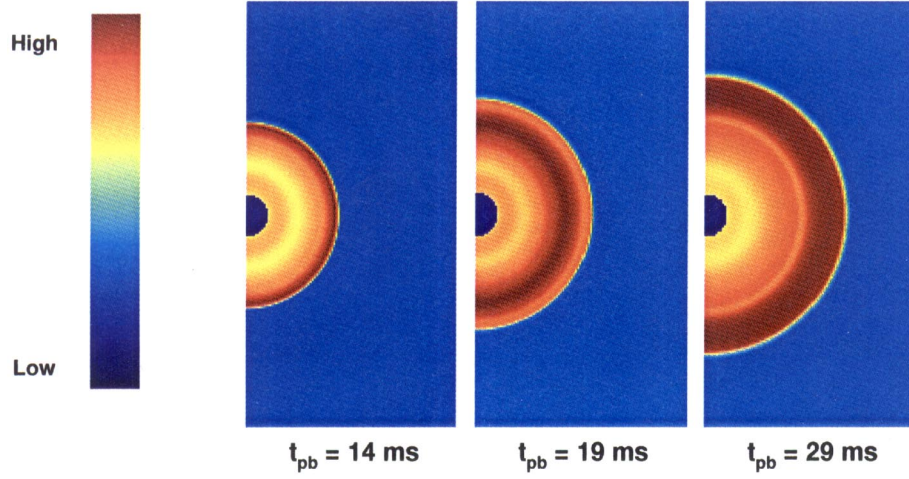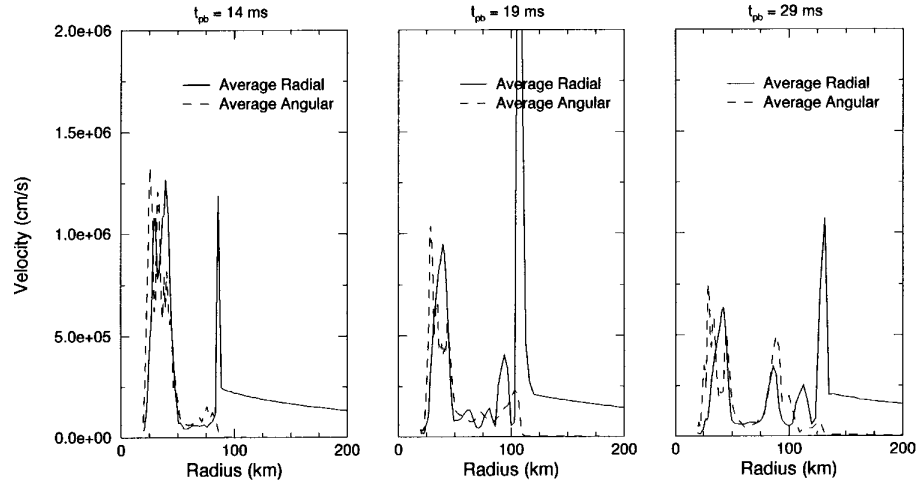
FIG. 4a

FIG. 4b

FIG. 4.—(a) Two-dimensional plots showing the entropy evolution of the 25 $M_\odot$ model in a simulation with neutrino transport (simulation D). (b) Plots of the angle-averaged radial and angular convection velocities corresponding to the three entropy snapshots in (a). (c) Plots showing the angle-averaged entropy and electron fraction profiles corresponding to the three entropy snapshots in (a). (d) Plot of the angle-averaged radial velocities in the innermost region of the two-dimensional grid for our fiducial 25 $M_\odot$ and 15 $M_\odot$ simulations (D and L).

MEZZACAPPA et al. (see 493, 855)

PLATE 36

FIG. 4c

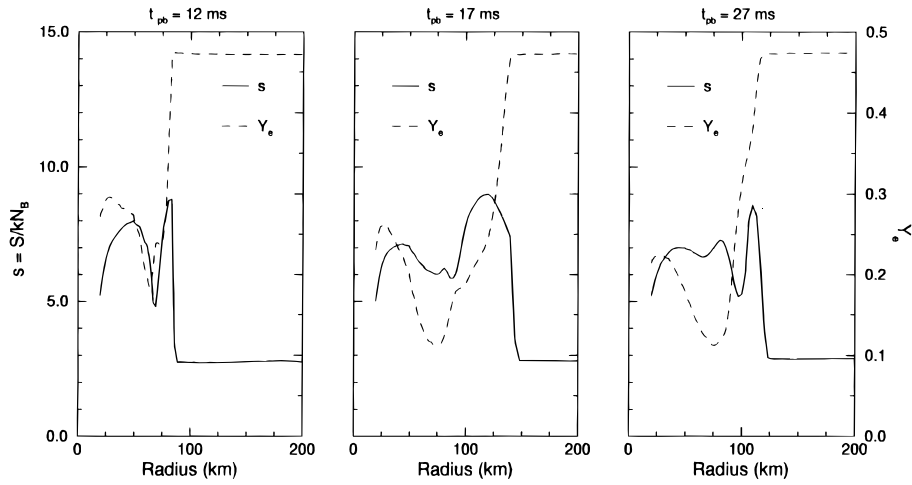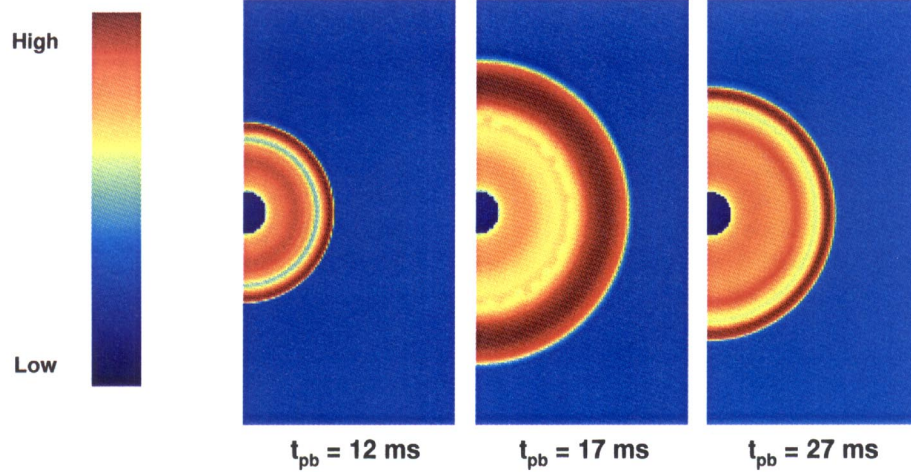## 25 M_Solar   15 M_Solar
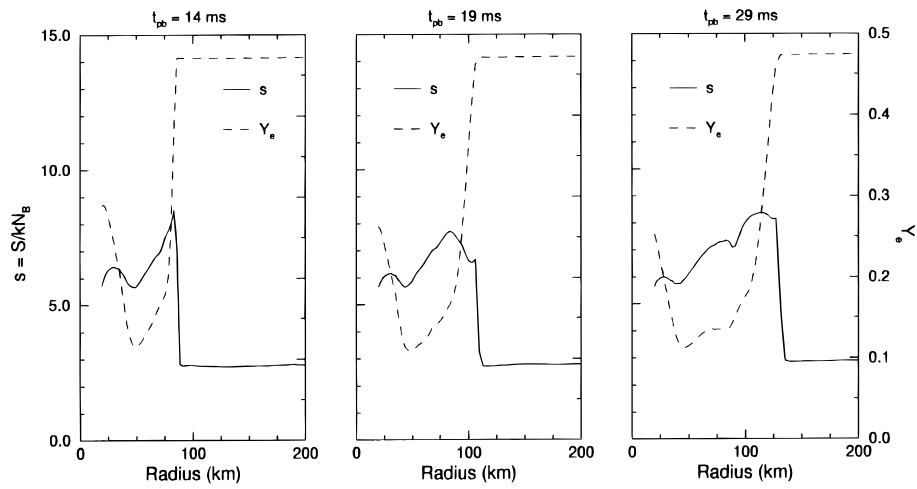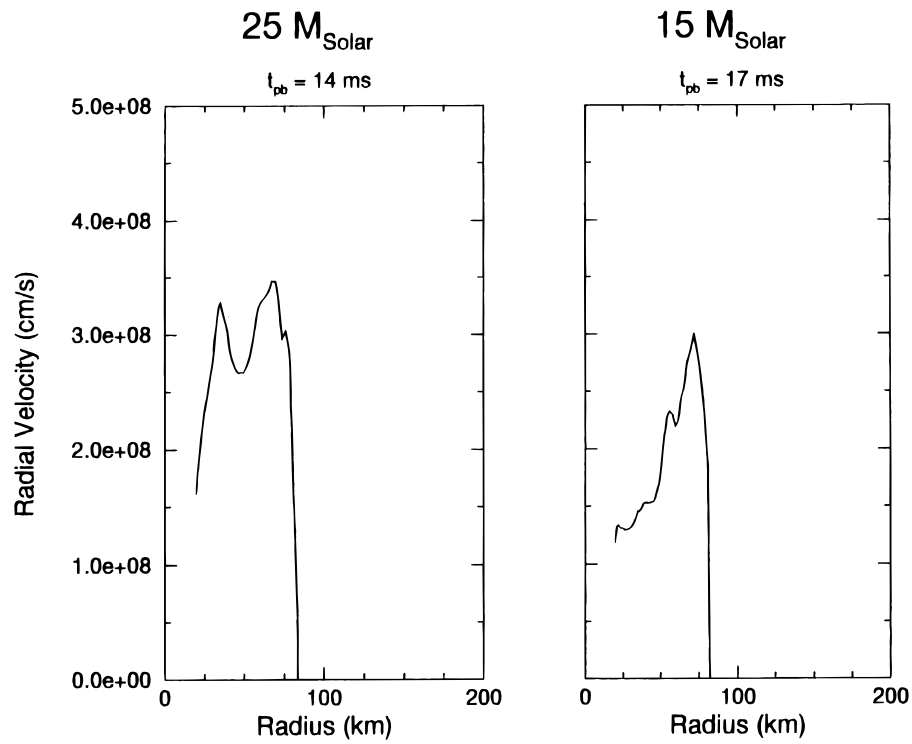
FIG. 4d

FIG. 5a

FIG. 5b

FIG. 5c

FIG. 5.—(a) Two-dimensional plots showing the entropy evolution of the 25 $M_\odot$ model in a simulation with neutrino transport that includes finite-time effects (simulation E). (b) Plots of the angle-averaged radial and angular convection velocities corresponding to the three entropy snapshots in (a). (c) Plots showing the angle-averaged entropy and electron fraction profiles corresponding to the three entropy snapshots in (a).

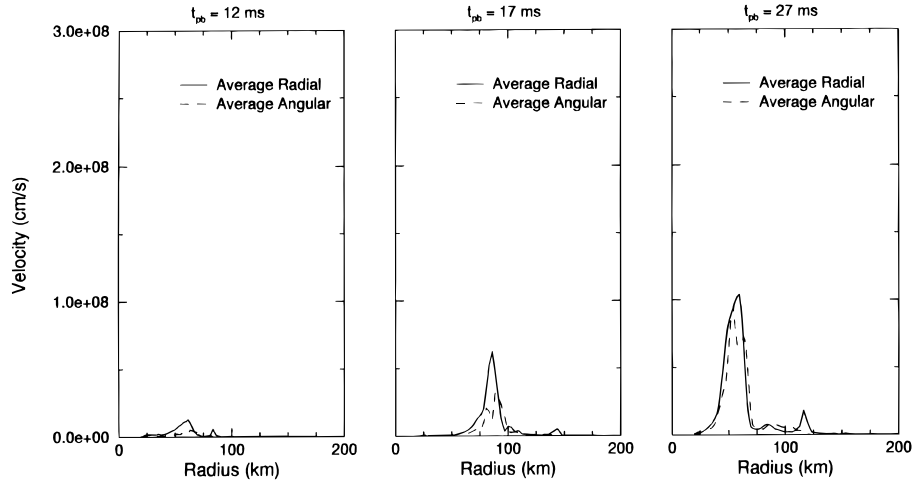MEZZACAPPA et al. (see 493, 858)

PLATE 38

FIG. 6a

FIG. 6b

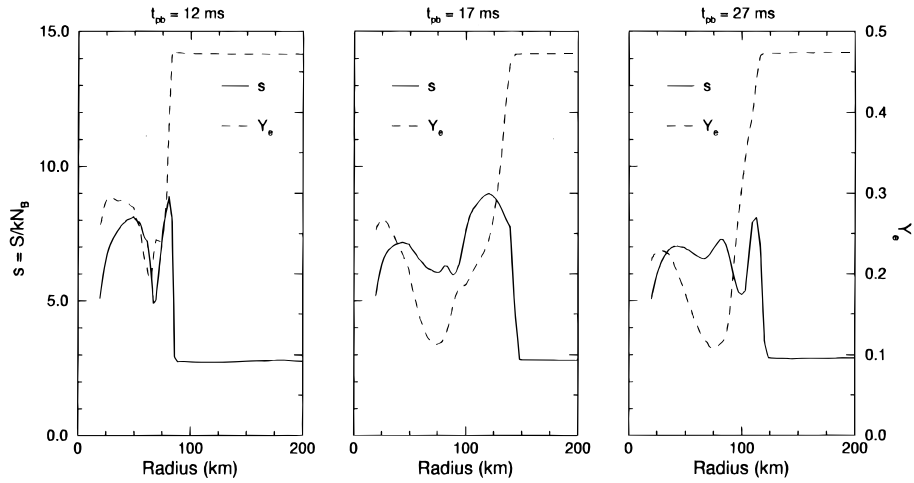
FIG. 6c

FIG. 6.—(a) Two-dimensional plots showing the entropy evolution of the 25 $M_\odot$ model in a simulation without neutrino transport that begins with low-test initial conditions (simulation F). (b) Plots of the angle-averaged radial and angular convection velocities corresponding to the three entropy snapshots in (a). (c) Plots showing the angle-averaged entropy and electron fraction profiles corresponding to the three entropy snapshots in (a).

MEZZACAPPA et al. (see 493, 858)

PLATE 39
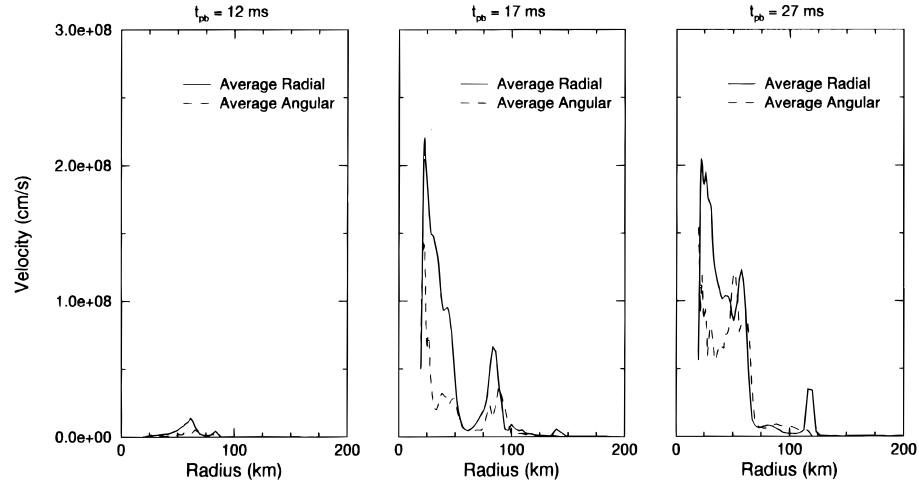
FIG. 7a

FIG. 7b

FIG. 7c

FIG. 7.—(a) Two-dimensional plots showing the entropy evolution of the 25 $M_\odot$ model in a simulation with neutrino transport that begins with low-test initial conditions (simulation G). (b) Plots of the angle-averaged radial and angular convection velocities corresponding to the three entropy snapshots in (a). (c) Plots showing the angle-averaged entropy and electron fraction corresponding to the three entropy snapshots in (a).
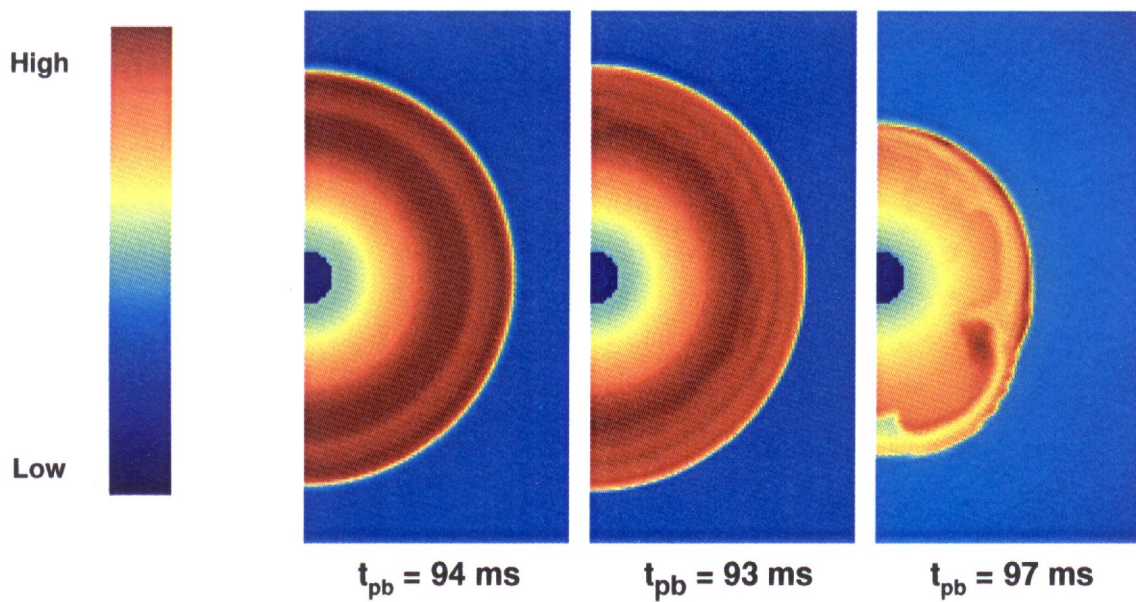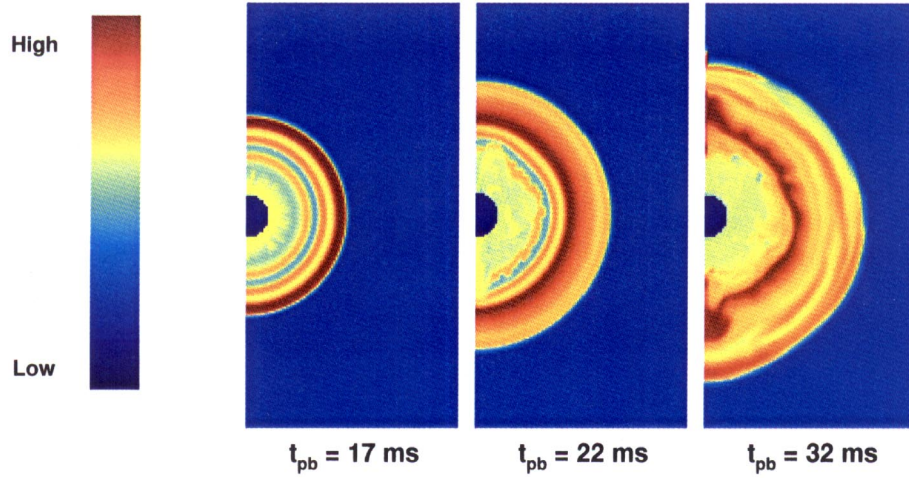
MEZZACAPPA et al. (see 493, 858)

PLATE 40

FIG. 8a

FIG. 8b

FIG. 8c

FIG. 8.—(a) Two-dimensional plots showing the entropy evolution of the 25 $M_\odot$ model in a simulation with neutrino transport that includes finite-time effects and begins with low-test initial conditions (simulation H). (b) Plots of the angle-averaged radial and angular convection velocities corresponding to the three entropy snapshots in (a). (c) Plots showing the angle-averaged entropy and electron fraction profiles corresponding to the three entropy snapshots in (a).

MEZZACAPPA et al. (see 493, 858)

PLATE 41

High

Low

$t_{pb} = 94$ ms $t_{pb} = 93$ ms $t_{pb} = 97$ ms

Fig. 9.—Two-dimensional entropy plots from simulations D, E, and G, at "late" times
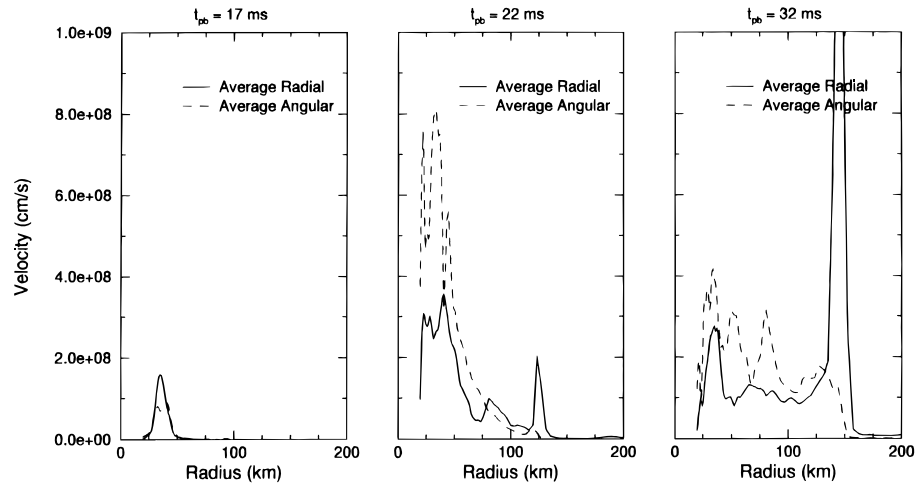
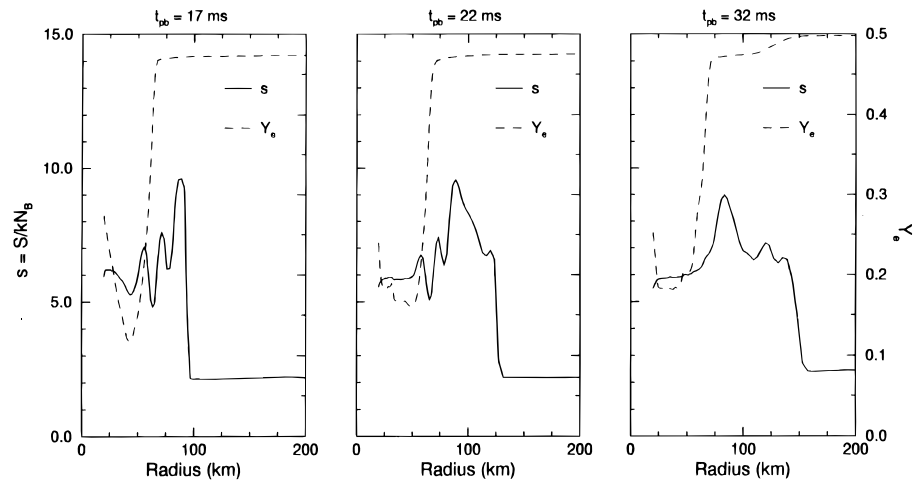Mezzacappa et al. (see 493, 858)

PLATE 42

FIG. 10a

FIG. 10b

FIG. 10c

FIG. 10.—(a) Two-dimensional plots showing the entropy evolution of the 15 $M_\odot$ model in a simulation without neutrino transport (simulation K). (b) Plots of the angle-averaged radial and angular convection velocities corresponding to the three entropy snapshots in (a). Plots showing the angle-averaged entropy and electron fraction profiles corresponding to the three entropy snapshots in (a).
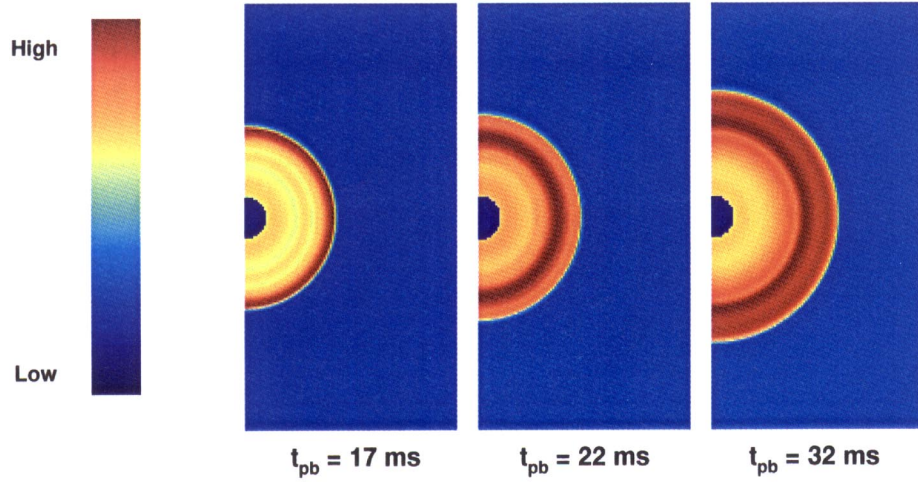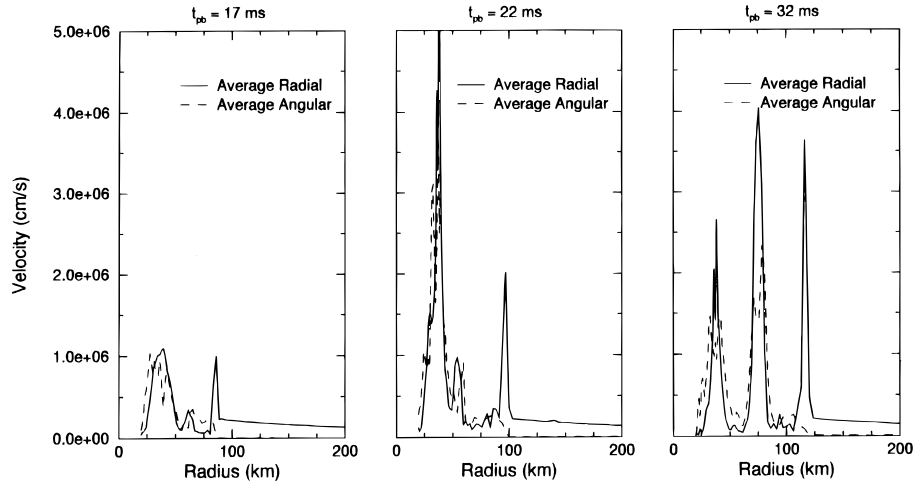
MEZZACAPPA et al. (see 493, 858)

PLATE 43

FIG. 11a

FIG. 11b
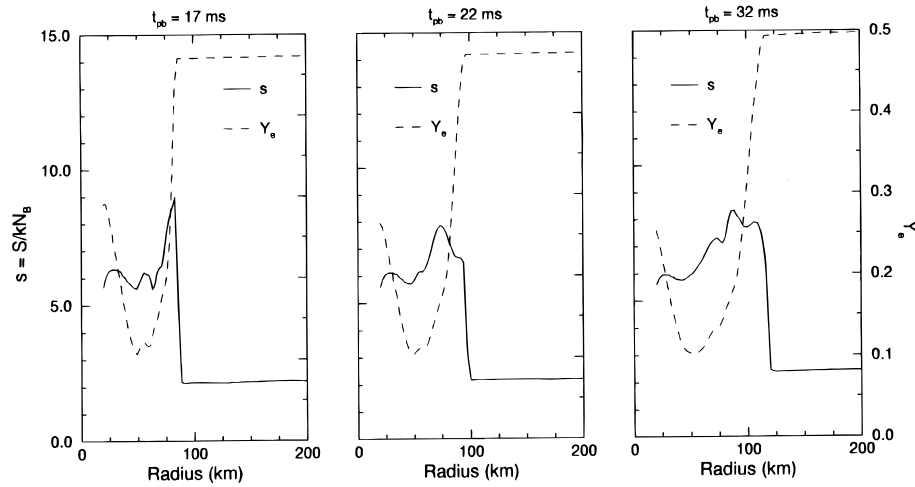

FIG. 11c

FIG. 11.—(a) Two-dimensional plots showing the entropy evolution of the 15 $M_\odot$ model in a simulation with neutrino transport (simulation L). (b) Plots of the angle-averaged radial and angular convection velocities corresponding to the three entropy snapshots in (a). (c) Plots showing the angle-averaged entropy and electron fraction profiles corresponding to the three entropy snapshots in (a).

MEZZACAPPA et al. (see 493, 858)

PLATE 44